THE EFFECT OF INDUCED STRESS HETEROGENEITY IN PORE SPACE

ON SOLID SUBSTITUION

A DISSERTATION

SUBMITTED TO THE DEPARTMENT OF GEOPHYSICS

AND THE COMMITTEE ON GRADUATE STUDIES

OF STANFORD UNIVERSITY

IN PARTIAL FULFILLMENT OF THE REQUIREMENTS

FOR THE DEGREE OF

DOCTOR OF PHILOSOPHY

Sabrina Aliyeva

December 2017

This dissertation is online at: http://purl.stanford.edu/bk865vf2070

I certify that I have read this dissertation and that, in my opinion, it is fully adequate in scope and quality as a dissertation for the degree of Doctor of Philosophy.

Gerald Mavko, Primary Adviser

I certify that I have read this dissertation and that, in my opinion, it is fully adequate in scope and quality as a dissertation for the degree of Doctor of Philosophy.

Jack Dvorkin

I certify that I have read this dissertation and that, in my opinion, it is fully adequate in scope and quality as a dissertation for the degree of Doctor of Philosophy.

Tapan Mukerji

Approved for the Stanford University Committee on Graduate Studies.

Patricia J. Gumport, Vice Provost for Graduate Education

This signature page was generated electronically upon submission of this dissertation in electronic format. An original signed hard copy of the signature page is on file in University Archives.

Abstract

In this dissertation, we introduce a new approach of predicting effective elastic properties upon solid substitution using strain energy and reciprocity theory. We confirm that the exact solution for fluid and solid substitution requires parameters that depend on pore geometry; therefore, substitution is *non-unique* if only pore-fill volume fraction is known. Using the new equations, which require less computational simulation as compare to a previous study (Saxena and Mavko, 2013) we find that the difference between pore geometry parameters stays *unchanged* in the same pore compliance. Hence, using this assumption we can predict effective elastic properties upon fluid and solid substitution. After introducing our approach, we discuss methods for obtaining the parameters of stress heterogeneity in the pore space. Finally, we demonstrate the new approach using an actual data set and accompanying 3D CT-scan image.

Since information about pore geometry is often unavailable, we present bounds to approximate pore geometry parameters for our new approach. Our new approach suggests a range of possible solutions with a final pore filling material. The range of

soft to stiff pore filling material substitution can be interpreted as maximum when there is large strain heterogeneity in the pore space and minimum when there is strain homogeneity in the pore space. When there is a stiff to soft pore filling material substitution, then, the range of possible solutions can be explained as the maximum change corresponds to strain homogeneity in the pore space and minimum change corresponds to strain heterogeneity in the pore space.

We also extend our *exact* substitution relations to substitute *porosity* in isotropic rocks. These new solutions are also equivalent to relaxing the assumption of unchanging rock microstructure upon substitution – a core assumption in the current models. Both the pore-filling phase and rock microstructure can change due to diagenesis, dissolution, precipitation, partial freezing or melting, etc., and these situations can be modeled using the new approach. We show that for two different pore compliances of any arbitrary pore shape, the difference in volume averaged stress heterogeneity in the pore spaces remains the same. This assumption is consistent with numerical simulations conducted on digital samples of the Fontainebleau and Berea sandstones.

We, also, study four different effective medium theory (EMT) models: Self-Consistent (SC), Differential Effective Medium (DEM), Mori-Tanaka (MT), and Kuster-Toksoz (KT). We plot a wide range of different aspect ratios (AR) for each model between Hashin-Shtrikman bounds (HS) to analyze certain gaps. We also perform fluid and solid substitution for each model. We, then, compare results to understand the change in effective bulk and shear moduli. Using recently derived

exact solid substitution equations by Saxena and Mavko (2013) we can analyze which model captures more heterogeneity in the pore space.

Finally, we find Comsol Multiphysics as a convenient tool for our numerical simulations. In this dissertation, we also show how problem of meshing complex geometry, such as we see in real rock, can be solved using Simpleware. The computations illustrate the challenges of estimating effective elastic properties on small samples. We observe that displacement boundary conditions tend to give moduli that are too stiff, and stress boundary conditions tend to give moduli that are too soft. We explored an embedding strategy by using a numerical "jacket" around the sample. A liquid jack transmits pressure boundary conditions to the inner rock sample, even though displacement boundary conditions are applied to the jacket.

Acknowledgement

I would like to express my sincere appreciation to my advisor, Gary Mavko for having so much faith in me. His inspiration and motivation were always effective and crucial in my academic life. Thanks for accepting me as your student, inspiring me, teaching me and allowing my weird schedule.

I am grateful to Jack Dvorkin for teaching me rock physics from his own unique perspective. Special thanks for helping me write my very first publication and getting my first internship.

I would like to thank Tapan Mukerji for helping me solve tricky problems in my research. He would always dedicate his time to explain and help me. I highly admire his enormous amount of knowledge. I feel very lucky that I could collaborate with Tapan during my research.

I thank Jenny Suckale for her thorough review and constructive comments on my dissertation.

I would also like to thank Donald R Lowe for agreeing to be my committee chair

I am also very grateful to Barbara Mavko for her exceptional kindness.

Thanks to Rachael Madison, Tara Arenas, Nancy Massarweh, and, Jared Gregory for helping me so much with all the paper works.

My colleagues made the last six years at Stanford special. I acknowledge all members of the SRB family. Thanks to Tiziana, Adam (Allan), Jane, Yu, Piyapa, Dario, Amos, Stéphanie, Chisato, Yuki, Ammar, Pinar, Abrar, Humberto, Amrita, Salma, Danica, and Iris. Special thanks to my office mates Natt and Vishal. My friends Noha, Abdul, Uri and Priyanka who made coffee and lunch breaks more fun. I am really grateful to Nishank Saxena for his mentorship in my first years at Stanford, his work and hourly long discussions truly inspired me.

The tremendous support of my family and friends helped me to go through rough patches of not only graduate school but personal life. Special mention to my dear friends, Raj, Momo, Nishank and Mrinalini.

I deeply thank my husband, Dibyendu who has been always by my side during some difficult decisions. My son, Rohan, is the main energy for me to face the tough days and enjoy the good ones. Finally, I would like to dedicate this dissertation to my mother, Marina and father, Teymur. They gave all the love and support, I could not have finished my PhD without them.

Contents

x

List of Tables

List of Figures

Chapter 1

Introduction

1.1 Motivation

Discovering oil is the ultimate prize in oil exploration; however, drilling a well can cost up to 500 million dollars, often causing significant environmental damage. Hence, it is of extreme importance to accurately predict the location of the oil reservoir before starting to drill. Using seismic waves (sonar waves) to scan the subsurface provides an economical method to get a general image of the whole exploration area structure. Looking at the images provided by the seismic waves, the best assumption is made to drill the first well (exploration well); however, in most cases, the prospect turns out to be a water filled reservoir. Rock physics models use the exploration well data to predict how

the seismic images would look like if this reservoir were filled with oil instead. One of the challenging problems in rock physics is to predict whether a reservoir is filled with a solid material such as heavy oil or bitumen. Most existing models are not applicable for this problem because of the underlying assumptions, which are insufficient to account for entirely different physical properties of solids as compared to fluids (water, oil, light-oil). Hence, the objective of this thesis is to study how heterogeneous porous medium filled with different materials physically respond to seismic waves saturated with a viscous material.

Gassmann's (1951) equations are often used for fluid substitution, the exercise of predicting the change in low-frequency seismic velocities upon substitution (or replacement) of ideal fluids (gas, water, light-oil, etc.) that fully saturate interconnected rock pores. If the medium is isotropic and the wave-induced stress is homogeneous, then Gassmann's equations are exact. However, in naturally occurring rock that have viscous or solid pore filling material such as bitumen, heavy oil, magma, or glycerol, these equations are no longer applicable, because these materials do not behave in a near-ideal manner: i.e., they do not instantly flow and they can support shear tractions at the pore boundaries when loaded at finite rates. Ciz and Shapiro (2007) modified Gassmann's equations for solid-saturated rocks by dropping the parameters that describe pore geometry, which were generally unknown. Ciz and Shapiro suggested an approximate equation that replaced the pore geometry parameter with the elastic properties of the pore-filling material. Recent findings by Makarynska et al. (2010) suggest that the accuracy of this approximation is very limited. Makarynska et al. (2010) also report that

although using the self-consistent approach (Berryman, 1992) improves the predictions, the results are not satisfactory. More recently, a new set of equations were derived by Saxena and Mavko (2013) which are different from the approximations suggested by Ciz and Shapiro. These exact equations make use of *pore geometry parameters*, that are presented in a computationally convenient form. However, this approach requires computational estimation of four unknown parameters. The main goal of this thesis is to introduce an alternative method for quantifying stress heterogeneity in the pore space and hence, reduce the number of unknown parameters. The new parameters will also provide a smaller range of solutions.

The theories of Gassmann, Brown and Korringa, and Ciz and Shapiro are fundamentally limited to substitution scenarios in which pore geometry does not change. This assumption limits the applicability of the theories to problems such as modeling digenesis (Avseth et al., 2005), estimating the effects of dissolution/precipitation (Hoefiner and Le Guen et al., 2007; Vanorio et al., 2011; Vialle and Vanorio, 2011), and modeling the effect of steam injection on heavy oil reservoirs (Schmitt, 1999; Bianco et al., 2008; Chopra et al., 2010).

In this thesis, we also target to predict the changes in effective bulk and shear moduli upon substitution of any pore filling material and the change in porosity for any arbitrary pore shape.

1.2   Chapter organization

In chapter 2, we explain how to estimate the effective elastic properties of a porous medium using numerical simulations. We discuss results found using Comsol Multiphysics™ for effective bulk and shear modulus estimation. We find that appropriately meshing the complex geometry, which is a necessary step in numerical simulations, is not always possible in Comsol Multiphysics. We find that another commercial software package – Simpleware™ -- is more useful for meshing the complex geometries that we see in real rocks. The known issue of overestimating estimated effective elastic properties using numerical simulations is also discussed in this chapter.

In chapter 3, we derive a new approach to modeling fluid-to-solid substitution for an elastic isotropic composite using strain energy and reciprocity theory. We also demonstrate that the volume averaged induced stress heterogeneity within the pore space remains relatively constant for any arbitrary pore shape if we stay within the same rock domain. Finally, we test the new approach using an actual data set and accompanying 3D CT-scan images.

In chapter 4, we extend our solid/fluid substitution equations (discussed in chapter 3) to solid/fluid substitution along with a change in porosity. We use our newly derived approach to describe solid/fluid substitution in isotropic elastic composites with arbitrary pore geometries.

In chapter 5, we introduce the bounds for obtaining pore geometry parameters in the case when a 3D CT-scan image is not available. The bounds are obtained using the Hashin-Shtrikman bounds. The only geometric input required for this rigorous method is

the pore volume fraction. The bounds method seems to accurately constrain the possible change in rock stiffness upon fluid or solid substitution in two phase isotropic rocks.

Chapter 6, we focus on four different Effective Medium Theory models: Self-Consistent (SC), Differential Effective Medium (DEM), Mori-Tanaka (MT), and Kuster-Toksöz (KT). We explore the limits of each model by comparing their predictions with the Hashin-Shtrikman bounds. We also compare results of how each model performs using fluid and solid substitution. Using the recently derived *exact* solid substitution equations by Saxena and Mavko (2013) we can analyze which model captures more accurately the heterogeneity in the pore space.

1.3   References

Biot, M.A., 1941, General theory of three-dimensional consolidation, Journal of Applied Physics, 12, 155-164.

Biot, M.A., 1956, Theory of propagation of elastic waves in a fluid saturated porous solid. I Low frequency range, The Journal of the Acoustical Society of America, 28, 168-178.

Biot, M.A., 1956, Theory of propagation of elastic waves in a fluid saturated porous solid. II Higher frequency range. The Journal of the Acoustical Society of America, 28, 179-191.

Biot, M.A., 1962, Mechanics of deformation and acoustic propagation in porous media, Journal of Applied Physics, 33, 1482-1498

Berryman, J. G., 1992, Effective stress for transport properties of inhomogeneous porous rock: Journal of Geophysical Research, 97, 17409–17424.

Ciz, R., and S., A., Shapiro, 2007, Generalization of Gassmann equations for porous media saturated with a solid material, Geophysics, 72, A75–A79.

Chapman, M., S. V. Zatsepin, and S. Crampin, 2002, Derivation of a microstructural poroelastic model: Geophysical Journal International, 151, 427–451.

Dvorkin, J., G. Mavko, and A. Nur, 1995, Squirt flow in fully saturated rocks, Geophysics, 60, 97–107.

Gassmann, F., 1951, Über die Elastizität poröser Medien: Vierteljahrschrift der Naturforschenden Gessellschaft in Zürich, 96, 1-23.

Hoefiner, M. L., and H. S. Fogler, 1988, Pore evolution and channel formation during flow and reaction in porous media: AIChE Journal, **34**, 1, 45–54.

Keehm, Y., Computational Rock Physics: Transport Properties in Porous media and applications, PhD Thesis, Stanford University, California, 2003.

Le Guen, Y., F. Renard, R. Hellmann, E. Brosse, M. Collombet, D. Tisserand, and J.P. Gratier, 2007, Enhanced deformation of limestone and sandstone in the presence of high PCO2 fluids: Journal of Geophysical Research, 112, B05421.

Mavko, G., and D. Jizba, 1991, Estimating grain-scale fluid effects on velocity dispersion in rocks, Geophysics, 56, 1940–1949.

Mavko, G., and A. Nur, 1975, Melt squirt in the asthenosphere: Journal of Geophysical Research, 80, 1444–1448.

Makarynska, D., Gurevich, B., Behura J., and Batzle, M., 2010, Fluid substitution in rocks saturated with viscoelastic fluids, Geophysics, **75**, E115-E122.

O'Connell, R., and Budiansky, B., 1977, Viscoelastic properties of fluid-saturated cracked solids, Journal of Geophysical Research, 82, 36, 5719-5735.

Sain, R., 2010, Numerical simulation of pore-scale heterogeneity and its effects on elastic, electrical and transport properties: PhD thesis, Stanford University.

Sahay, P., 1996, Elastodynamics of deformable porous media, Proceedings of Royal Society London, 452, 1517-1529.

Sahay, P., Spanos, T., and V. de la Cruz, 2001, Seismic wave propagation in inhomogeneous and anisotropic porous media, Geophys. J. Int., 145, 209-222.

de la Cruz, Spanos, T., 1985, Seismic wave propagation in a porous medium, Geophysics, 50, 1556-1565.

de la Cruz, Sahay, P., Spanos, T., 1993, Thermodynamics of Porous Media, Mathematical and Physical Science, 443, 1917.

Vanorio, T., G. Mavko, S. Vialle, and K. Spratt, 2010, The rock physics basis for 4D seismic monitoring of CO_2 fate: Are we there yet?: The Leading Edge, **29**, 156.

Vanorio, T., A. M. Nur, and Y. Ebert, 2011, Rock physics analysis and time-lapse rock imaging of geochemical effects due to the injection of CO2 into reservoir rocks: Geophysics, in review.

Vialle, S., and T. Vanorio, 2011, Laboratory measurements of elastic properties of carbonate rocks during injection of reactive CO2-saturated water: Geophysical Research Letters, **38**, L01302.

Yeong, C. L. Y. and Torquato, S., 1998, Reconstructing random media. II. Three-dimensional media from two-dimensional cuts, Physical Review E, 58, 224-233.

Chapter 2

Numerical Simulations

2.1.   Abstract

Most of my thesis work is based on numerical simulations, hence, this chapter is dedicated to explanation on how numerical simulations are performed in order to estimate the effective elastic properties of a porous media. In particular, we find that it is convenient to use Comsol Multiphysics for effective bulk and shear modulus estimation. We argue how problem of complex geometry, such as we see in real rock, can be solved using Simpleware. Known issue of stiffer computationally estimated effective elastic properties is also discussed in this chapter.

2.2. Introduction

Computation of physical properties on 3-D CT-scanned digital rocks is used in geosciences applications, and a number of different workflows and algorithms have become available. We discuss a study on elasticity in different rock types (Figure 2.1) using Simpleware, and Comsol Multiphysics code. The 3D CT-scan images of different rock types are Berea Sandstone and Fontainebleau Sandstone (Figure 2.1). The materials for the grains and pore-fill assumed for the study are water and quartz with the following elastic properties and conductivities:

Table 2.1. Elastic properties, conductivity and viscosity

Material	Young's Modulus (GPa)	Poisson Ratio
Water	3e-9	0.49
Quartz	94.5	0.08

Berea Sandstone
voxel – 5.35 μm

Fontainebleau Sandstone
voxel – 7.5 μm
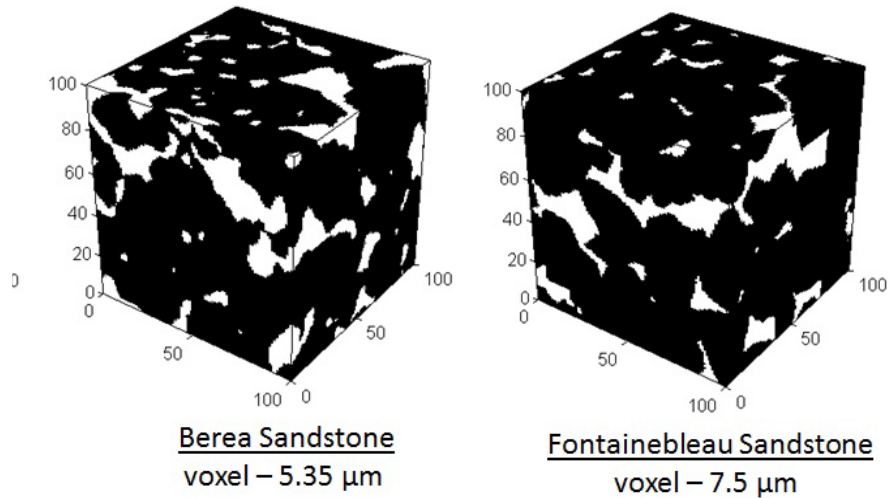
Figure. 2.1. 3D CT scan volumes of size 100x100x100. Black color here is a solid matrix and white color is pore space.

2.3.   Assembly of real rocks

Comsol Multiphysics^{TM} software is widely used to analyze potential rock physics properties at the macro scale. However, running Comsol simulations on a real rock sample is a challenging due to lack of a good FEM meshing option in this particular software. However, using Simpleware^{TM} software we are able to first generate a mesh representing a wide range of rock geometries and then import those meshes in Comsol for physical property simulation. In this chapter I discuss a recipe for using this process.

We start by importing the 3D scanned image volumes of each sample into Simpleware ScanIP (Synopsys, Mountain View, USA) for image processing and segmentation. Since all of the 3D scan volumes used in this discussion are 100x100x100, each cube consists of 100 2D images of 100x100 size. We perform meshing using the Simpleware +FE-Free meshing algorithm with tetrahedral elements. Since the rock model is based on a pre-segmented image (a binary image without any greyscale information reflecting the sub-voxel geometry of the sample), it is best to select the "Binarise before smoothing" option. In this way the meshing algorithm in Simpleware does not try to use any spurious greyscale information that might have been introduced into masks by thresholding, and the generated mesh has porosity closer to that of the original image.
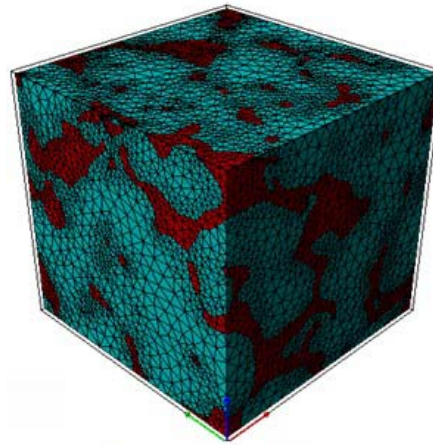
Figure. 2.2. Typical 3D CT scan volumes of size 100x100x100.

We perform meshing using the Finite Element mesh algorithm with the tetrahedral element type and threshold of coarseness of -45, which limits edge length between 3.65 and 9.1 of corresponding unit length. Figure 2.2 shows an example of meshing Berea sandstone. An example of a finer mesh of the same pore structure is shown in Figure 2.3.
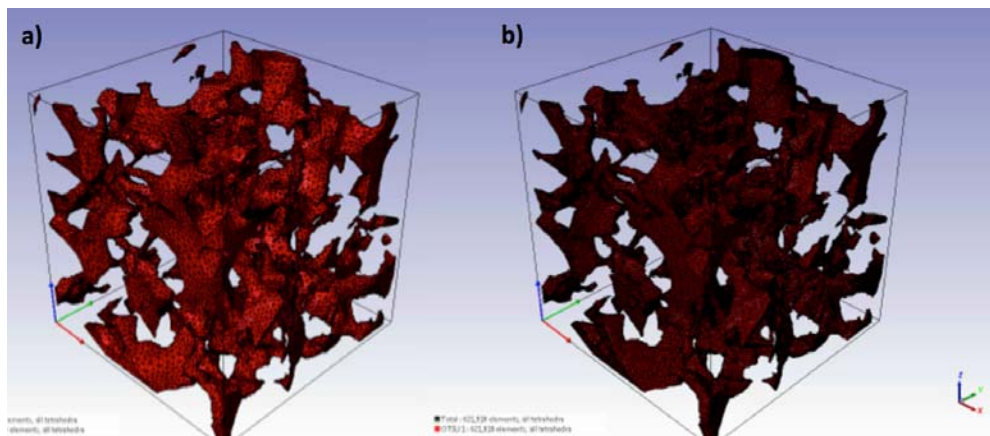
Figure. 2.3. 3D mesh of pore structure of Fontainebleau sample: a) has a mesh size parameter of -25 (coarser than voxel size) resulting in 165,933 tetrahedral elements. b) has a mesh size parameter of 0 (same as the voxel size) resulting in 621,918 tetrahedral elements.

2.4. Numerical computations of effective elastic properties

We import the Simpleware mesh of each of the sample, into Comsol, which solves the relevant partial differential equations to estimates the desired physical properties.

The relevant partial differential equations (elastostatic, electrical conduction, and Stoke's flow) are solved in Comsol using the finite element method. To compute effective elastic properties in Comsol, we use the Solid Mechanics package and assign Linear Elastic Material for each domain. In this research, we use only two domains: the first domain is mineral matrix and the second domain is pore space. For material properties of each phase, we work with bulk and shear modulus. It is necessary to mention that if air/gas is used as one of the domain materials, then bulk and shear moduli have to be very small positive values and not zero. We usually use 1Pa for both bulk and shear modulus for air/gas.

2.5. Boundary Conditions for Effective Bulk Modulus

We apply normal prescribed displacements in the Boundary System to estimate the effective bulk modulus. Usually the displacement has to be a very small value compared with the sample size, since we want to simulate far field infinitesimal strain boundary conditions; hence, we use displacements -1e-6 units of pixel size. The negative sign means that we compress 3D cube. The general idea of this process is illustrated on Figure 2.4. The effective bulk modulus is then computed by taking the ratio of volume integration over the mean normal stress and volumetric strain.
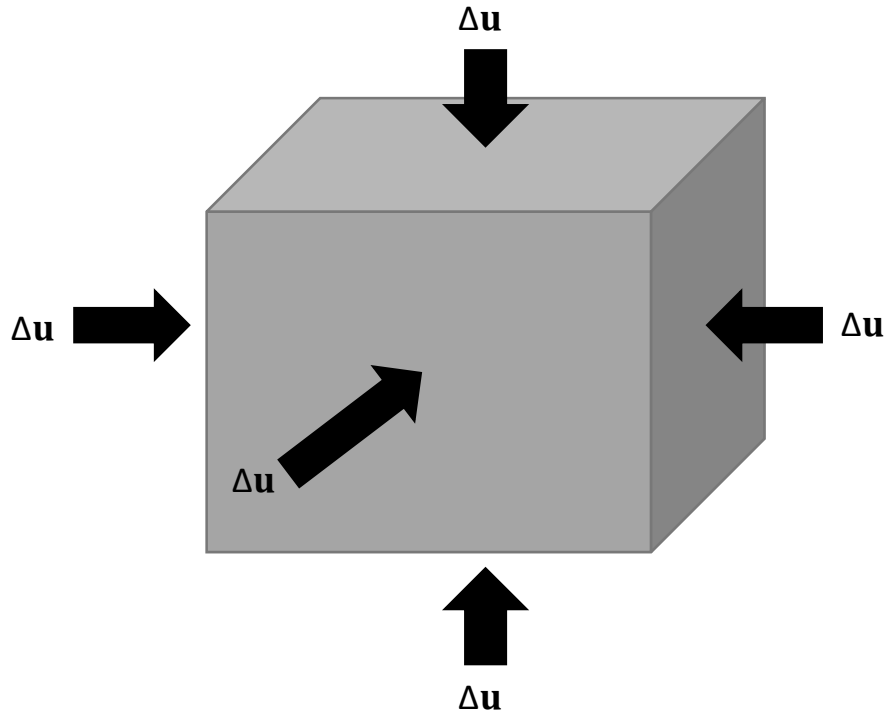
Figure 2.4: Normal displacement is applied on the boundaries of a 3D cube.

2.6. Boundary Conditions for Effective Shear Modulus

To estimate effective shear modulus, we apply a series of sliding displacements in the Global Coordinate System. As in the effective bulk modulus problem, we use tangential displacement magnitude of -1e-6 units of pixel size. In order to estimate the effective shear modulus in Comsol we use **simple** shear boundary conditions. Unlike in normal boundary condition, there is no direct method to apply **simple** shear boundary conditions in Comsol. Hence, we use four separate Prescribed Displacements in Solid Mechanics Study. On Figure 2.5 we show the general idea of simple shear boundary conditions. There are three visible surfaces of the cube: A, B and C and three opposite surfaces: A', B' and C'. The coordinate system is shown in right low corner of Figure 2.5. Essentially,

we want to tangentially pull the sides of the cube (highlighted in red color); hence, surface B has to move in direction –Y and surface A' – in direction X. Surface A slides in direction –X and surface B' – in direction Y. In a perfectly isotropic medium, surfaces C and C' will have zero normal displacements; therefore, we apply a Rolling constraint on these surfaces, which allows for tangential displacement but no normal displacement. Since we pull sides of the cube in X-Y directions, the effective shear modulus is computed by taking the ratios of volume integration over the shear stresses and shear strains in the X-Y planes.
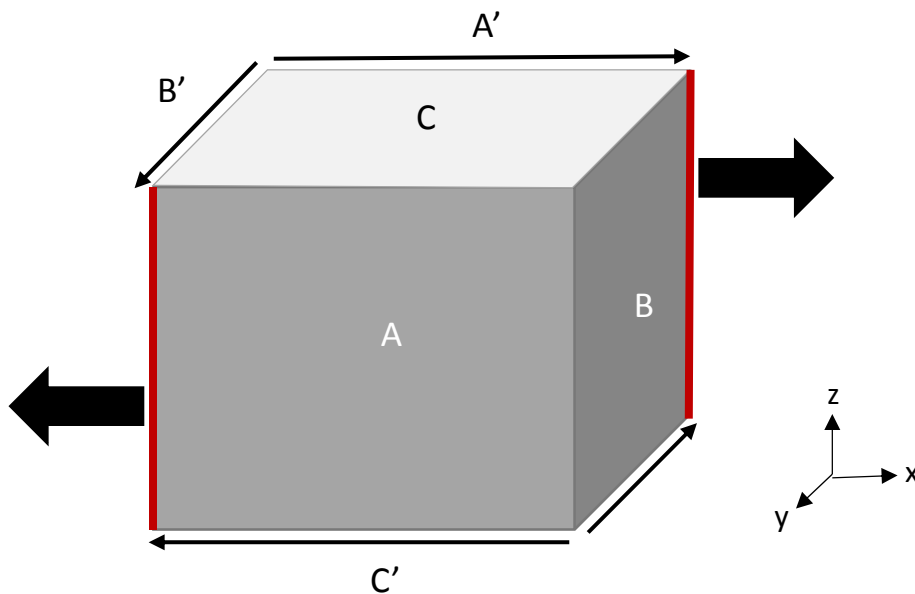
Figure 2.5: Simple shear displacement is applied on the boundaries of a 3D cube.

The CT scan volumes are shown in Figures 2.1 and 2.7, where the white color is the pore space and the black color is the mineral matrix. We computationally assign pore space to be water and mineral matrix to be quartz (sandstone scans). The properties for

each constituent material are used from Table 2.1 The corresponding effective elastic

moduli estimated using Comsol are shown in Table 2.2.

Table 2.2: Effective elastic properties using Comsol.

Effective Elastic moduli	Berea Sandstone	Fontainebleau Sandstone
Young's Modulus (GPa)	50.63	62.7
Poisson Ratio	0.12	0.12

2.7.   Comparison of numerical simulations with laboratory measurements

A general problem that we find with either of these tools is that the sample size is

often smaller than the representative element volume (REV); in sub-REV simulations

with displacement boundary conditions, the estimated stiffness is often too large --

approximately an upper bound on the desired effective moduli (Huet, 1990). An example

is shown on Figure 2.6. The black color squares are the laboratory measurements of

Berea sandstone (Han, 1986) and the red color circle is the COMSOL computational

simulation on the 3D CT scan image the size of 100^3 the pore space of which is saturated

with air (bulk modulus: 1 Pa, shear modulus: 1 Pa).
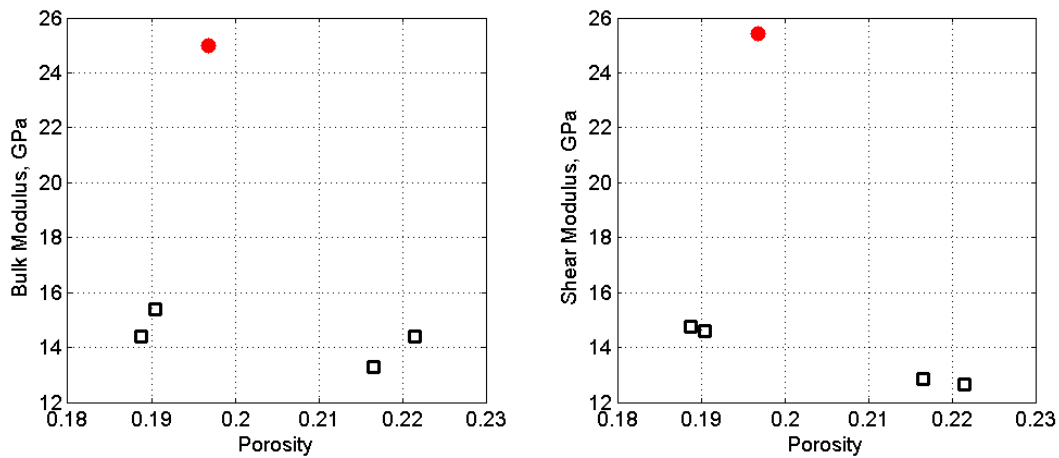
Figure 2.6: The end red color point is the Berea sandstone. The black empty square symbols are actual lab measurements (Han, 1986).

In order to overcome the general problem of stiffer computed effective elastic properties when using displacement boundary conditions, we use a "jacket" to soften computationally estimated effective elastic properties. This is sometimes called an "embedded" strategy (Böhm, 2008). In this study, the jacket is constructed by adding a layer of 5 extra pixels thick to each face of the 3D CT scan image. An example of this idea is shown on Figure 2.7. A slice is taken from Berea sandstone, where the pore space is shown in white, the solid matrix is in black, and the "jacket" is the red color around the rock.

Varying the jacket elastic properties weakens the effect of the displacement boundary condition. For example, a liquid jacket can only transmit hydrostatic stress to the surfaces of the inner rock sample. Therefore, even though we apply displacement boundary conditions to the jacket, the inner rock sample deforms as though there is a pressure boundary condition; In a sub-REV sample, this would yield a softer effective stiffness – approximately a lower bound on the effective modulus. Direct stress boundary

conditions in a finite element program can be unstable and requires constraining a point in the center of the cube to have zero displacement and zero rotation (which comes with a lot of challenges). The jacket strategy allows us to stay with the displacement boundary conditions.
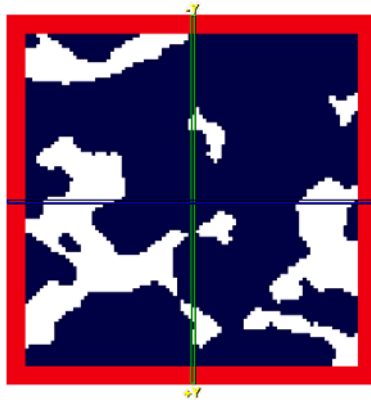
Figure 2.7: Example of a slice of 3D cube of jacketed (red color) CT scan rock image.

Figure 2.8 shows an example of computed stresses in a rock. On the right, the sample is unjacketed with normal displacement boundary conditions; on the left, normal displacement boundary conditions are applied using a liquid jacket. The pore space is saturated with air (Bulk modulus: 1 Pa, Shear modulus: 1 Pa); the solid matrix is quartz (Bulk modulus: 36 GPa, Shear modulus: 44 GPa); and the "jacket" material is liquid (Poisson's ratio: 0.49, Young's modulus: 0.5 GPa).
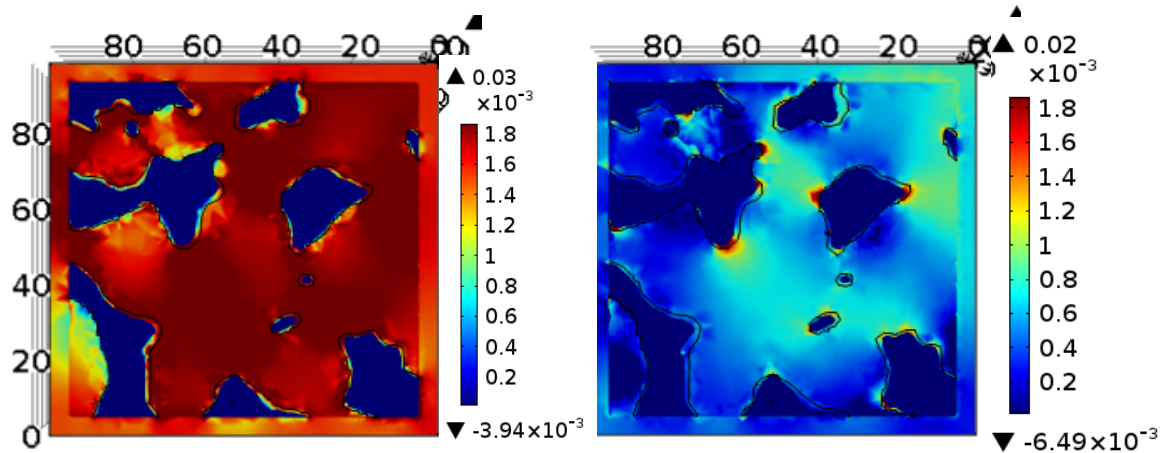
Figure 2.8: Figure on the left is an example of stresses in a rock with direct stress boundary conditions. Figure on the right is an example of stresses in a rock with displacement boundary conditions applied to a liquid jacket surrounding the sample.

To study what material properties of the "jacket" are suited for our work, we run a range of different material properties from liquid to solid. We vary Young's modulus from 0.5 GPa to 50 GPa and Poisson's ratio from 0.49 to 0.19. All of the material properties are shown on Table 2.3. We use 3 different sandstone 3D CT scan images: Berea sandstone, Fontainebleau sandstone and Cenovus oil sand. We compare our computational simulations with laboratory measures for Berea sandstone and Fontainebleau sandstone and well log data for Cenovus oil sand. For all of our 3D CT scan images we use quartz for the solid matrix (Bulk modulus: 36 GPa, Shear modulus: 44 GPa). For Berea sandstone and Fontainebleau sandstone the pore space is specified with air (Bulk modulus: 1 Pa, Shear modulus: 1 Pa), and for Cenovus we use cold heavy oil (Bulk modulus: 3.2 GPa, Shear modulus: 0.5 GPa). As a result, we show (Figure 4 and 5) 15 computational simulations of effective bulk and shear modulus using different material properties of jacket in black-colored stars, effective elastic moduli using direct

displacement boundary conditions without a jacket in red-colored point, and laboratory measurements (Han, 1986) or well log data with black empty square symbol. The x-axis on the figures is just the simulation sample number. With the increase in sample number on the x-axis, the material moduli of the "jacket" increases according to the Table 2.3.

Table 2.3: A range of material properties of "jacket".

	Young's Modulus GPa	Poisson Ratio
1	0.50	0.49
2	4.04	0.47
3	7.57	0.45
4	11.11	0.42
5	14.64	0.40
6	18.18	0.38
7	21.71	0.36
8	25.25	0.34
9	28.79	0.32
10	32.32	0.29
11	35.86	0.28
12	39.39	0.25
13	42.93	0.23
14	46.46	0.21
15	50.00	0.19

On Figures 2.9 and 2.10 we show computationally estimated effective bulk and shear modulus of Berea and Fontainebleau sandstone, respectively. We notice that computationally estimated effective elastic properties with much softer "jacket" match the laboratory measures of Berea sandstone (Han, 1986). (The "measured" moduli are

extracted from measured ultrasonic P- and S-wave velocities. The red points are the computationally estimated effective bulk and shear moduli computed *without* a "jacket". Note that the unjacketed and jacketed moduli agree when the jacket material is stiff.
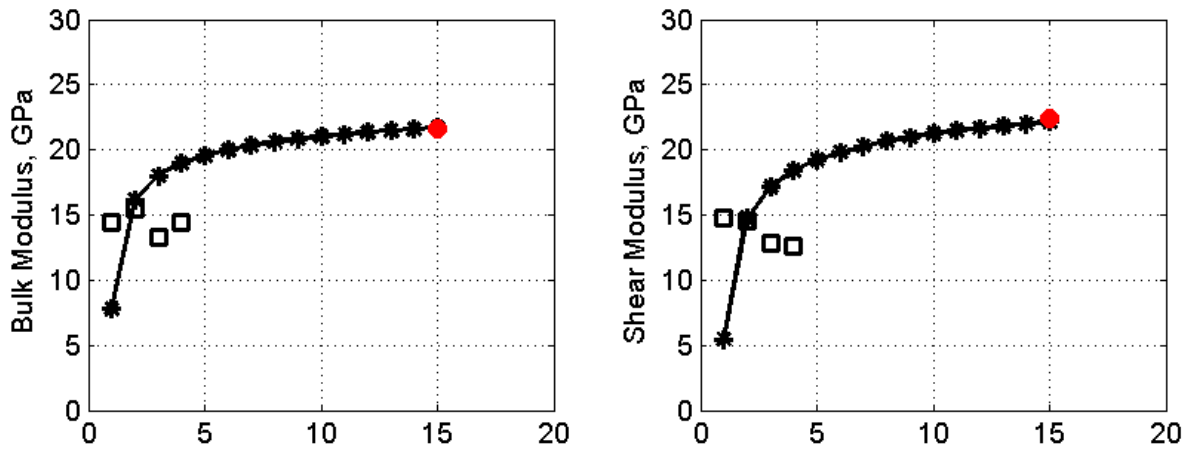
Figure 2.9: 15 simulations of different material properties of "jacket" used with Berea sandstone and shown in black color stars. The end red color point is the Berea sandstone with direct stain boundary conditions. The black empty square symbols are actual lab measurements (Han, 1986).
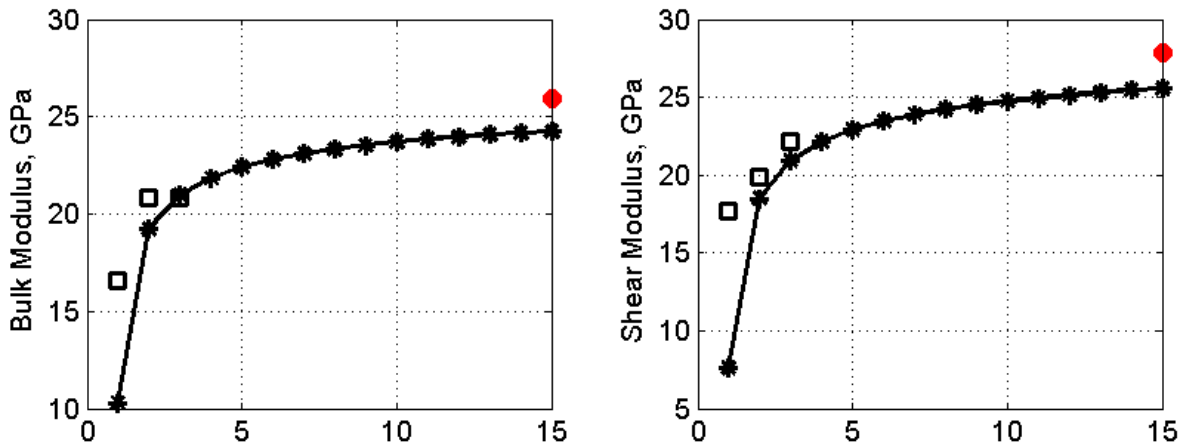
Figure 2.10: 15 simulations of different material properties of "jacket" used with Fontainebleau sandstone and shown in black color stars. The end red color point is the Fontainebleau sandstone with direct stain boundary conditions. The black empty square symbols are laboratory measurements (Han, 1986).

On Figure 2.11 we show computationally estimated effective bulk and shear modulus of Cenovus oil sand. We notice that the data point from a well log data, which is saturated with cold heavy oil, falls below computationally estimated effective elastic properties with much softer "jacket"; however it falls on the same trend. The red points are the computationally estimated effective bulk and shear modulus *without* "jacket", which gives stiffer results, matching the effective elastic properties with "jacket", when the jacket is stiffest.
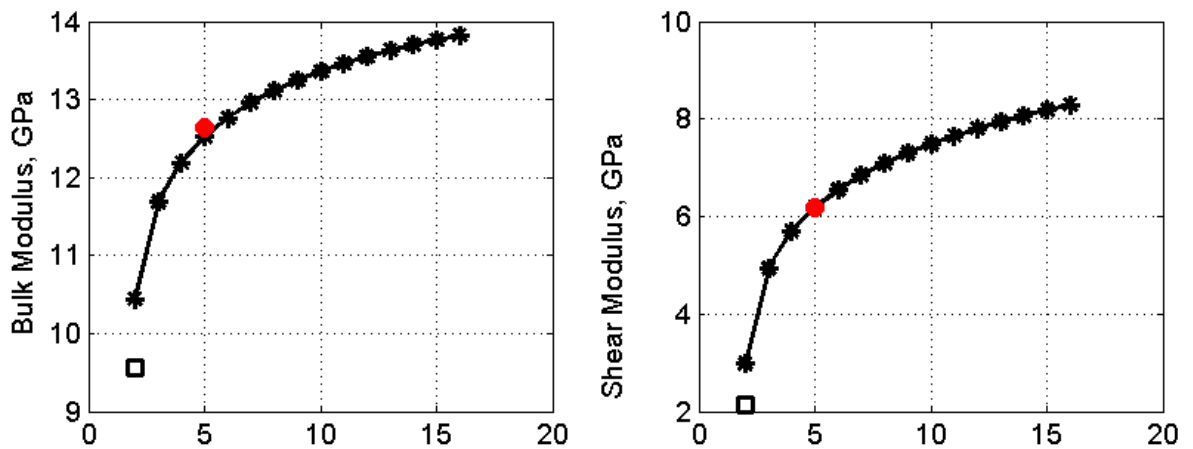
Figure 2.11: 15 simulations of different material properties of "jacket" used with Cenovus oil sand and shown in black color starts. The end red color point is the Berea sandstone with direct stain boundary conditions. The black empty square symbol is taken from well log data.

As a conclusion from this small study we decided to use 5 GPa of Young's modulus and 0.47 of Poisson Ratio as material properties of "jacket" for our future computational simulations.

2.8. Chapter Summary

Simpleware is widely used in meshing complex rock geometries. Comsol is a reliable FEM solver -- it provides more outputs than just effective properties, such as the internal distributions of field variables (e.g. stress, strains, electrical fields, flow vectors etc.). It allows more control over the conditions of the problem but in general the computations can be slow. Sometimes with a very fine mesh, Comsol runs out of the memory (on the particular hardware used) and does not converge.

The computations illustrate the challenges of estimating effective elastic properties on small samples. In sub-REV samples, displacement boundary conditions tend to give moduli that are too stiff, and stress boundary conditions tend to give moduli that are too soft. We explored an embedding strategy by using a numerical "jacket" around the sample. A liquid jack transmits pressure boundary conditions to the inner rock sample, even though displacement boundary conditions are applied to the jacket. Our computed moduli are closer to the laboratory values when the jacket is soft; precise choice of the best jacket properties requires calibration.

2.9. Acknowledgements

2.10. References

Andra H, N. Combaret, E. Glatt ,J. Han , M. Kabel , Y. Keehm , F. Krzikalla, 2013 Digital rock physics benchmarks—Part I: *Imaging and segmentation. Computers & Geosciences 50 (2013) 25–32.*

Böhm, H.J., 2008, A short introduction to basic aspects of continuum micromechanics, ILSB Report / ILSB-Arbeitsbericht 206 (supersedes CDL{FMD report 3{1998)

Dong H., 2007 Micro-CT imaging and pore network extraction. *PhD Dissertation. Imperial College, London*

Garboczi E. J. *1998* Finite element and finite difference programs for computing the linear electric and elastic properties of Digital images of random materials *National Institute of Standards and Technology.*

Huet, C., 1990, Application of variational concepts to size effects in elastic heterogeneous bodies, Journal of the Mechanics and Physics of Solids, 38, 813-841.

Keehm, Y., T. Mukerji, and A. Nur (2004), Permeability prediction from thin sections: 3D reconstruction and Lattice-Boltzmann flow simulation, Geophys. Res. Lett., 31, L04606

Youngseuk Keehm, Tapan Mukerji, and Amos Nur (2001) Two-phase flow in complex porous media using Lattice-Boltzmann method. *SEG Technical Program Expanded Abstracts 2001:* pp. 1724-1727.

Chapter 3

Equations for fluid and solid substitution

3.1. Abstract

In this chapter we use strain energy and reciprocity theory to introduce a new approach to modeling fluid-to-solid substitution for an elastic isotropic composite. In addition, we show that for a constant pore compliance, volume averaged stress heterogeneity in the pore space remains the same for any arbitrary pore shape. Our approach can be used for any pore filling material as long as we account for stress heterogeneity in the pore space. After introducing our approach, we discuss methods for obtaining the parameters of stress heterogeneity in the pore space. Finally, we demonstrate the new approach using an actual data set and accompanying 3D CT-scan image.

3.2. Introduction

Fluid substitution is most often described using Gassmann's (1951) equations, which relate the fluid-saturated composite bulk and shear moduli of a porous material with the dry composite moduli. For isotropic homogeneous rocks, Gassmann's equations depend only on the bulk modulus of the elastic mineral and the initial effective bulk modulus, porosity, and bulk modulus of the pore fluid. For fluid-saturated rocks, Gassmann's equations are exact as long as the induced volumetric stress in the pore space is homogeneous.

Ciz and Shapiro (2007) modified Gassmann's equations for solid-saturated rocks by dropping the pore geometry parameters, which were generally unknown. They proposed the approximate solid substitution equations

$$\frac{K_{sat1}}{K_m - K_{sat1}} - \frac{K_{p_1}}{\phi(K_m - K_{p_1})} \approx \frac{K_{sat2}}{K_m - K_{sat2}} - \frac{K_{p_2}}{\phi(K_m - K_{p_2})} \quad , \qquad (3.1)$$

and

$$\frac{G_{sat1}}{G_m - G_{sat1}} - \frac{G_{p_1}}{\phi(G_m - G_{p_1})} \approx \frac{G_{sat2}}{G_m - G_{sat2}} - \frac{G_{p_2}}{\phi(G_m - G_{p_2})} \quad . \qquad (3.2)$$

In Eqns. 3.1 and 3.2, ϕ is the porosity, K_{p_1} and G_{p_1} are the bulk and shear moduli of the initial pore-filling solid, K_{p_2} and G_{p_2} are the bulk and shear moduli of the final pore-filling solid, K_m and G_m are the bulk and shear moduli of the mineral in the rock frame, K_{sat1} and G_{sat1} are the effective bulk and shear moduli of the initial-filled composite, and K_{sat2} and

G_{sat2} are the effective bulk and shear moduli of the final-filled composite. In cases where $G_p = 0$, Eqns. 3.1 and 3.2 reduce to Gassmann's equations. More recently, Saxena and Mavko (2013) derived *exact* solid substitution equations that differ from the approximations suggested by Ciz and Shapiro. These exact equations make use of *pore geometry parameters*, which are presented in a computationally convenient form. For fluid-to-solid substitution of the bulk modulus,

$$\left(K_{p_1} - K_{p_2}\right)\alpha_1 + \left(G_{p_1} - G_{p_2}\right)\alpha_2' = \phi\frac{\left(K_m - K_{p_2}\right)\left(K_m - K_{p_1}\right)}{\left(K_m - K_{sat1}\right)\left(K_m - K_{sat2}\right)}\left(K_{sat1} - K_{sat2}\right) \qquad , \qquad (3.3)$$

where

$$\alpha_1 = \frac{\overline{P^{p_1} P^{p_2}}}{P^{p_1} P^{p_2}} \quad \alpha_2 = \frac{1}{2}\frac{\overline{\tau_{ij}^{p_1}\tau_{ij}^{p_2}}}{P^{p_1} P^{p_2}} \qquad ,$$

and

$$\alpha_2' = \frac{K_{p_1} K_{p_2}}{G_{p_1} G_{p_2}}\alpha_2 \qquad ,$$

where α_2' depends on α_2.

For effective shear modulus

$$\left(G_{p_1} - G_{p_2}\right)\beta_1 + \left(K_{p_1} - K_{p_2}\right)\beta_2' = \phi \frac{\left(G_m - G_{p_2}\right)\left(G_m - G_{p_1}\right)}{\left(G_m - G_{sat2}\right)\left(G_m - G_{sat1}\right)}\left(G_{sat1} - G_{sat1}\right) \qquad , \qquad (3.4)$$

where

$$\beta_1 = \frac{1}{2} \frac{\overline{\tau_{ij}^{p_1} \tau_{ij}^{p_2}}}{\tau_{12}^{p_1} \tau_{12}^{p_2}} \qquad \beta_2 = \frac{\overline{P^{p_1} P^{p_2}}}{\tau_{12}^{p_1} \tau_{12}^{p_2}} \qquad ,$$

and

$$\beta_2' = \frac{G_{p_1} G_{p_2}}{K_{p_1} K_{p_2}} \beta_2 \qquad .$$

In the Eqns. 3.3 and 3.4, $P^{p_{1,2}}$ is the volumetric induced stress in the initial and final pore filling materials, respectively, and $\tau_{ij}^{p_{1,2}}$ is the shear-induced stress in the initial and final pore filling materials, respectively ($\overline{\Psi}$ denotes the pore volume average of parameter Ψ). It is guaranteed that α_1, $\beta_1 \geq 1$ and α_2, $\beta_2 \geq 0$.

We derive a new approach for describing solid substitution in isotropic elastic composites with arbitrary pore geometries. Our ultimate goal is to reduce the computational expense and introduce an alternative method for quantifying stress heterogeneity in the pore space. This will provide a smaller range of solutions for pore geometry parameters.

3.3. Substitution Equations

In this section, we derive substitution equation for effective bulk and shear moduli. We, then, show a comparison between new derivations and numerically estimated effective bulk and shear moduli of Berea and Fontainebleau sandstone samples.

3.3.1. Bulk Modulus Derivation
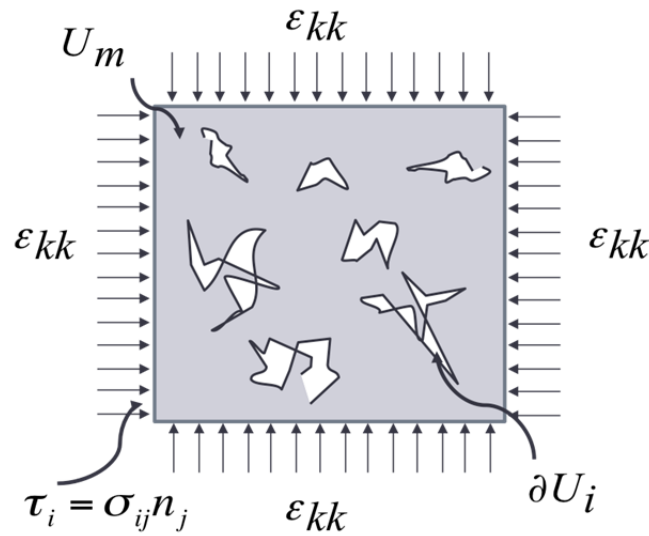
Figure 3.1: Compressional tractions on an arbitrary pore shape composite.

Let an isotropic and homogenous elastic body on Figure 3.1 be subjected to volumetric surface traction as

$$\tau_i = \sigma_{ij} n_j \qquad , \tag{3.5}$$

where τ_i are surface traction components, σ_{ij} is a constant stress tensor with equal principal values, and n_j are normal vectors to the outer surface. Then the strain energy U stored in the elastic body is given as

$$U = \frac{1}{2}\int_S \tau_i u_i dS = \frac{1}{2}\int_V \sigma_{ij}\varepsilon_{ij} dV$$

where u_i is the displacement acting on the surface of the body, and stress σ_{ij} and strain ε_{ij} are connected by Hooke's law:

$$\sigma_{ij} = K\varepsilon_{kk}\delta_{ij} + 2G(\varepsilon_{ij} - \frac{1}{3}\varepsilon_{kk}\delta_{ij}) \qquad . \tag{3.6}$$

These stresses and strains can be also described as

$$\sigma_{ij} = -P\delta_{ij} + T_{ij} \qquad , \tag{3.7}$$

and

$$\varepsilon_{ij} = \varepsilon_{kk}\delta_{ij} + \gamma_{ij} \qquad , \tag{3.8}$$

where P is normal stress or pressure (negative of mean stress, $-\sigma_{kk}/3$), T_{ij} are deviatoric stresses, ε_{kk} is volume strain, and γ_{ij} is deviatoric strain.

A number of inclusions of arbitrary shapes and elastic moduli K_p and G_p are added into the homogenous body. The strain energy stored in the inclusions is given by

$$\partial U_p = \sum_{n=1}^{N} U_{p_n} \qquad . \tag{3.9}$$

If the *same* surface tractions are applied to the new isotropic elastic composite, it has been shown by Eshelby (1951, 1956) that the difference in elastic energy stored in the two cases is given by

$$\partial U_p = U - U_m = \frac{1}{2}\int_S \left(\tau_i \overline{u_i^p} - \overline{\tau_i^p} u_i \right) dS \qquad , \tag{3.10}$$

where U is the strain energy stored in the elastic composite and U_m is the strain energy stored in the elastic body without inclusions. $\overline{S}$ is the surface of the inclusion, and $\overline{\tau_i^p}$ and $\overline{u_i^p}$ are the traction and displacement vectors on the surface of the inclusion.

Subscript '*p*' refers to inclusions in the composite, and '*m*' refers to the body loaded by the same tractions *without* inclusions; values with no subscript refer to the effective properties of the composite loaded by the same traction.

The strain energy stored in the pore space is expressed as

$$\partial U_p = \frac{1}{2}\int_S \left(\tau_i \overline{u_i^p} - \overline{\tau_i^p} u_i \right) dS = \frac{1}{2}\int_V \left(\frac{1}{K_p} - \frac{1}{K_m} \right) P_p P_m dV \qquad , \tag{3.11}$$

where P_p is the volumetric induced stress in the pore space (inclusions) and P_m is the volumetric induced stress in the same elastic body with no pore space (inclusions).

On the other hand, strain energy stored in the pore space can be written as

$$\partial U_p = \frac{1}{2}\left(\frac{P^2}{K} - \frac{P_m^{\,2}}{K_m} \right) V \qquad . \tag{3.12}$$

Since the composite of K_m is homogeneous, it guarantees that $P_m = P$:

$$\frac{1}{2}\int_V \left(\frac{1}{K_p} - \frac{1}{K_m} \right) P_p P dV = \frac{1}{2}\left(\frac{P^2}{K} - \frac{P_m^{\,2}}{K_m} \right) V \qquad . \tag{3.13}$$

Hence Eqn. 3.13 reduces to

$$\frac{\dfrac{1}{K} - \dfrac{1}{K_m}}{\phi\left(\dfrac{1}{K_p} - \dfrac{1}{K_m}\right)} = \frac{\overline{P_p}}{P} \quad , \tag{3.14}$$

where K is the effective bulk modulus of the rock, ϕ is the porosity, K_p is the modulus of the pore-filling material, and K_m is the solid frame modulus.

From Hooke's law,

$$P = K\varepsilon_{kk} \quad , \tag{3.15}$$

and

$$P_p = K_p\varepsilon^p{}_{kk} \quad , \tag{3.16}$$

where $\varepsilon^p{}_{kk}$ is volumetric strain in the pore space, which can be expressed using Eshelby's theory as

$$\varepsilon^p{}_{kk} = \overline{\theta_v}\varepsilon_{kk} \quad . \tag{3.17}$$

After rearranging the terms in Eqn. 3.14 we get

$$\frac{K_m - K}{\phi(K_m - K_p)} = \overline{\theta_v} \quad . \tag{3.18}$$

Parameter $\overline{\theta_v}$ is the volumetric strain concentration in the pore space, defined as the average strain in the pore space divided by the average strain in the rock. Certain properties of $\overline{\theta_v}$ are

known: for any arbitrary pore shape a general argument can be made for $1/\phi \geq \overline{\theta_v} > 1$. Parameter

$\overline{\theta_v}$ depends on the pore space geometry and the properties of the pore-filling material.

3.3.2. Shear Modulus Derivation

$$U_m \qquad \varepsilon_{ij}$$

$$\varepsilon_{ij} \qquad \qquad \varepsilon_{ij}$$

$$\tau_i = \sigma_{ij} n_j \qquad \varepsilon_{ij} \qquad \partial U_i$$
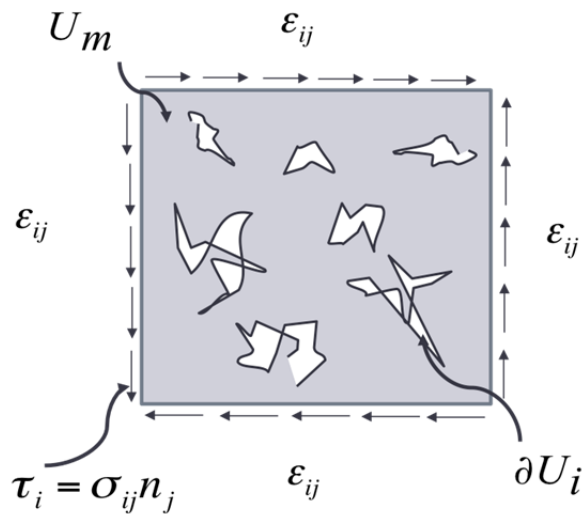
Figure 3.2: Shear tractions on an arbitrary pore shape composite.

Now let the same isotropic and homogenous elastic body on Figure 3.2 be subjected to shear

surface tractions as

$$\begin{pmatrix} \tau_1 \\ \tau_2 \\ \tau_3 \end{pmatrix} = \begin{pmatrix} 0 & T & 0 \\ T & 0 & 0 \\ 0 & 0 & 0 \end{pmatrix} \begin{pmatrix} n_1 \\ n_2 \\ n_3 \end{pmatrix} \qquad . \tag{3.19}$$

We drop the *ij* notation in deviatoric stress, assuming that $T_{12} = T_{21} = T$. In a composite loaded

by the these tractions, the strain energy stored in the pore space is expressed as

$$\frac{1}{2} \int_V \left(\frac{1}{G_p} - \frac{1}{G_m} \right) T_p T dV = \frac{1}{2} \left(\frac{T^2}{G} - \frac{T^2}{G_m} \right) V \qquad . \tag{3.20}$$

Rearranging terms and using the volume averaging notation we get

$$\frac{\dfrac{1}{G} - \dfrac{1}{G_m}}{\varphi\left(\dfrac{1}{G_p} - \dfrac{1}{G_m}\right)} = \frac{\overline{T_p}}{T} \qquad , \qquad (3.21)$$

Where G is the effective shear modulus of the rock, G_p is the pore-filling shear modulus,

and G_m is the shear modulus of the solid frame material.

Using Hooke's law,

$$T_{ij} = 2G\varepsilon_{ij} \qquad , \qquad (3.22)$$

and Eshelby's theory for shear strain ε^*_{ij} in the pore space,

$$T_{ij(p)} = 2G_p\varepsilon^*_{ij} \qquad , \qquad (3.23)$$

we rearrange Eqn. 3.21:

$$\frac{G_m - G}{\phi(G_m - G_p)} = \overline{\theta_d} \qquad . \qquad (3.24)$$

Eqn. 3.21 provides the exact effective shear modulus for any arbitrary pore shape. Parameter

$\overline{\theta_d}$, introduced in Eqn. 3.24, captures the concentration strain of induced shear stress in the pore

space. It is generally true that $1/\phi \geq \overline{\theta_d} > 1$. $\overline{\theta_d}$ also depends on pore shape and pore filling

material.

Consider an initial composite K_{sat1}, G_{sat1}, where frame K_m, G_m with pore space ϕ is

fully saturated with initial pore material K_{p_1}, G_{p_1}. We can write Eqn. 3.18 and 3.24 as

$$\frac{K_m - K_{sat1}}{\phi\left(K_m - K_{p_1}\right)} = \overline{\theta_v^{p_1}} \qquad , \qquad\qquad (3.25)$$

and

$$\frac{G_m - G_{sat1}}{\phi\left(G_m - G_{p_1}\right)} = \overline{\theta_d^{p_1}} \qquad , \qquad\qquad (3.26)$$

Next, we consider same composite saturated with a new pore filling material K_{p_2}, G_{p_2} and

estimate the new effective bulk and shear moduli:

$$\frac{K_m - K_{sat2}}{\phi\left(K_m - K_{p_2}\right)} = \overline{\theta_v^{p_2}} \qquad , \qquad\qquad (3.27)$$

and

$$\frac{G_m - G_{sat2}}{\phi\left(G_m - G_{p_2}\right)} = \overline{\theta_d^{p_2}} \qquad . \qquad\qquad (3.28)$$

Subtracting the equations for the final material, (3.27) and (3.28), from those for the initial

material, (3.25) and (3.26), we obtain

$$\frac{K_m - K_{sat1}}{\phi\left(K_m - K_{p_1}\right)} - \frac{K_m - K_{sat2}}{\phi\left(K_m - K_{p_2}\right)} = \overline{\theta_v^{p_1}} - \overline{\theta_v^{p_2}} \qquad , \qquad\qquad (3.29)$$

and

$$\frac{G_m - G_{sat1}}{\phi(G_m - G_{p_1})} - \frac{G_m - G_{sat2}}{\phi(G_m - G_{p_2})} = \overline{\theta_d^{p_1}} - \overline{\theta_d^{p_2}} \qquad . \tag{3.30}$$

As porosity changes, the effective bulk and shear moduli may also change; however, if porosity changes within the same pore compliance, then $\overline{\theta_v^{p_1}} - \overline{\theta_v^{p_2}}$ and $\overline{\theta_d^{p_1}} - \overline{\theta_d^{p_2}}$ are approximately constant.

$$\frac{K_m - K_{sat1}}{\phi(K_m - K_{p_1})} - \frac{K_m - K_{sat2}}{\phi(K_m - K_{p_2})} \approx C_v \qquad , \tag{3.31}$$

$$\frac{G_m - G_{sat1}}{\phi(G_m - G_{p_1})} - \frac{G_m - G_{sat2}}{\phi(G_m - G_{p_2})} \approx C_d \qquad . \tag{3.32}$$

If $K_{p_1} \leq K_{p_2}$ and $G_{p_1} \leq G_{p_2}$, then $K_{sat_1} \leq K_{sat_2}$, $G_{sat_1} \leq G_{sat_2}$ and $\overline{\theta_v^{p_2}} \leq \overline{\theta_v^{p_1}}$, $\overline{\theta_d^{p_2}} \leq \overline{\theta_d^{p_1}}$; hence, C_v and C_d must have non-negative values. Subscripts *"v"* and *"d"* denote boundary conditions of volumetric and deviatoric strain, respectively.

3.3.3. Comparison

To show that C_v and C_d are approximately constant within the same pore compliance we refer to Fontainebleau and Berea sandstone digital samples. Each sample is divided into 5 sub-samples. All of the sub-samples are relatively isotropic. Although the porosity of each sub-sample differs, the pore compliance stays the same for each original sample. From numerical

simulations, we obtain $\overline{\theta_v}$ and $\overline{\theta_d}$ for sub-samples saturated with water (bulk: 2.2 GPa, shear: 1

Pa) and heavy oil (bulk: 2.5 GPa, shear: 0.4 GPa), assuming that the mineral matrix is pure

quartz (bulk: 37 GPa, shear: 44 GPa). We then estimate $\overline{\theta_v^{water}} - \overline{\theta_v^{heavyoil}}$ and $\overline{\theta_d^{water}} - \overline{\theta_d^{heavyoil}}$.

C_v and C_d have approximately constant values for all 5 sub-samples of each sandstone digital

sample. The results are shown on Table 3.1 and 3.2 for the Fontainebleau and Berea sandstones,

respectively.

Table 3.1: A list of pore compliance parameters for the Fontainebleau sandstone.

Porosity	$\overline{\theta_v}$ water	$\overline{\theta_v}$ heavy oil	C_v	$\overline{\theta_d}$ water	$\overline{\theta_d}$ heavy oil	C_d
0.129	2.13	2.07	0.06	2.82	2.69	0.13
0.136	2.21	2.13	0.07	2.80	2.67	0.13
0.142	2.14	2.08	0.07	2.81	2.67	0.13
0.152	2.13	2.06	0.07	2.81	2.67	0.14
0.153	2.13	2.06	0.07	2.82	2.66	0.16

Table 3.2: A list of pore compliance parameters for the Berea sandstone.

Porosity	$\overline{\theta_v}$ water	$\overline{\theta_v}$ heavy oil	C_v	$\overline{\theta_d}$ water	$\overline{\theta_d}$ heavy oil	C_d
0.226	1.87	1.82	0.04	2.42	2.32	0.10
0.227	1.89	1.84	0.05	2.36	2.27	0.09
0.231	1.90	1.86	0.05	2.57	2.45	0.11
0.243	1.89	1.85	0.05	2.37	2.27	0.09
0.262	1.89	1.83	0.05	2.34	2.25	0.10

Figure 3.1 shows numerically computed effective bulk (K_{sat1}^{water}) and shear (G_{sat1}^{water}) moduli

for the Fontainebleau and Berea sandstones saturated with water (blue curves). The green curves

on Figure 3.1 show that using the constant values mentioned for Eqns. 3.31 and 3.32 provides

better predictions for water and heavy oil pore filling materials than do the Ciz and Shapiro

approximations (red curves).

We would like to predict the numerically estimated effective elastic properties of sandstones saturated with heavy oil $K_{sat2}^{heavyoil}$ and $G_{sat2}^{heavyoil}$ (black curves). To this end, Eqns. 3.31 and 3.32 can be written as follows:

Fontainebleau sandstone

$$\frac{K_{quartz} - K_{sat1}^{water}}{\phi(K_{quartz} - K_{water})} - \frac{K_{quartz} - K_{sat2}^{heavyoil}}{\phi(K_{quartz} - K_{heavyoil})} \approx 0.07$$

$$\frac{G_{quartz} - G_{sat1}^{water}}{\phi(G_{quartz} - G_{water})} - \frac{G_{quartz} - G_{sat2}^{heavyoil}}{\phi(G_{quartz} - G_{heavyoil})} \approx 0.13$$

Berea sandstone

$$\frac{K_{quartz} - K_{sat1}^{water}}{\phi(K_{quartz} - K_{water})} - \frac{K_{quartz} - K_{sat2}^{heavyoil}}{\phi(K_{quartz} - K_{heavyoil})} \approx 0.05$$

$$\frac{G_{quartz} - G_{sat1}^{water}}{\phi(G_{quartz} - G_{water})} - \frac{G_{quartz} - G_{sat2}^{heavyoil}}{\phi(G_{quartz} - G_{heavyoil})} \approx 0.10$$
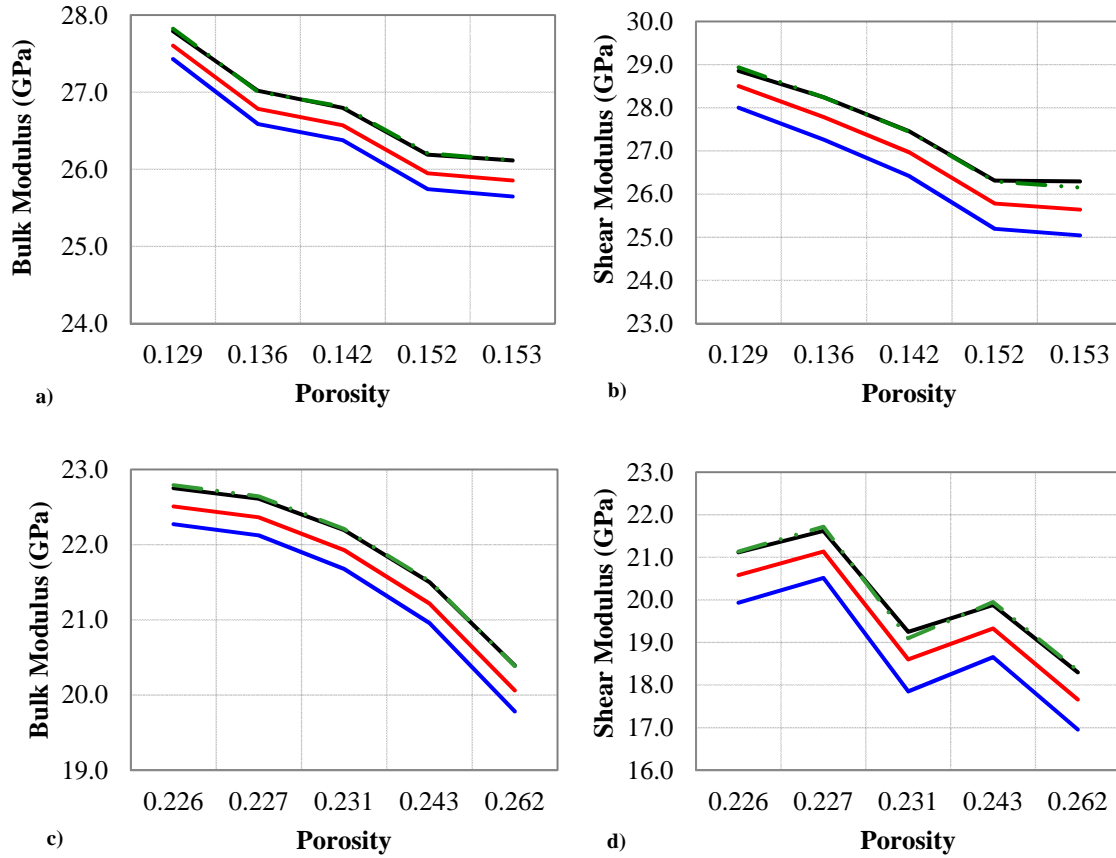
Figure 3.3: *Top row:* Fontainebleau sandstone: a) Effective bulk modulus, b) Effective shear modulus. *Bottom row:* Berea sandstone: c) Effective bulk modulus, d) Effective shear modulus. Blue color curves are numerically estimated effective elastic properties of sandstone sub-samples saturated with water. Black color curves are numerically estimated effective elastic properties of sandstone sub-samples saturated with heavy oil. Red color curves are substituted water with heavy oil pore filling material using the Ciz and Shapiro approximation. Green color curves are substituted water with heavy oil pore filling material using Eqns. 3.31 and 3.32.

Parameters $\overline{\theta_v}$ and $\overline{\theta_d}$ can be estimated computationally using a 3D CT-scan image or experimentally using laboratory measurements for *Vp* and *Vs* in a core sample. $\overline{\theta_v}$ and $\overline{\theta_d}$ depend on pore geometry and pore filling material. For computational and laboratory experiments it is necessary to estimate these parameters for a composite saturated with the final pore filling material. In computational simulations, parameters $\overline{\theta_v}$ and $\overline{\theta_d}$ can be obtained directly or by

using Eqns. 3.28 and 3.29 from K_{sat2} and G_{sat2}. In cases where neither a CT-scan image nor a core sample is available, these parameters can be approximated using $\overline{\theta_v}$ and $\overline{\theta_d}$ bounds.

3.4.   Application

To study the application of Eqns. 3.31 and 3.32 to real data, we use well log data and a 3D CT-scan image (Figure 3.4) from a reservoir saturated with heavy oil. We assume that pore compliance does not change in the interval of interest (an assumption required by our model).
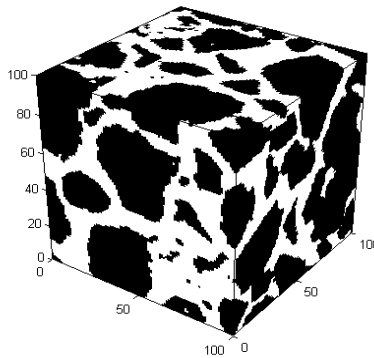
Figure 3.4: 3D CT-scan image of a sample containing quartz grains (black, bulk modulus: 37 GPa, shear modulus: 44 GPa) and heavy oil (white, bulk modulus: 3.2 GPa, shear modulus: 0.1 GPa)
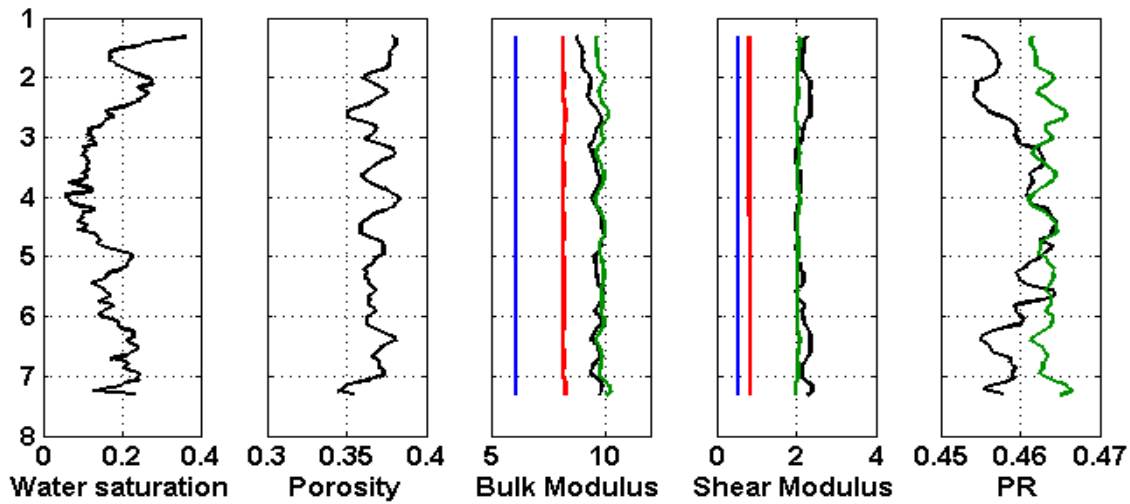
Figure 3.5: Model results vs well log data: Black curves show original well log data for an interval saturated with heavy oil. Blue curves are bulk and shear moduli numerically computed from a CT-scan image fully virtually saturated with water. Red curves are predicted bulk and shear moduli (bulk: 2.2 GPa and shear: 1Pa) for rocks fully saturated with heavy oil obtained using the Ciz and Shapiro approximation. Green curves are predicted bulk and shear moduli of rocks fully saturated with heavy oil obtained using Eqns. 3.22 and 3.23.

Imagine that we have water-saturated well log data and would like to predict the effective bulk and shear curves for heavy oil-saturated zones in the same rock (this will allow us to compare model results with actual well log data). First, we assume a pure quartz frame and use the available 3D CT-scan image to model the pore structure. After virtually saturating the model with water, we numerically apply volumetric strain and simple shear strain to estimate the effective bulk and shear moduli. Using Eqns. 3.25 and 3.26, we find $\overline{\theta_v^{p_1}}$ and $\overline{\theta_d^{p_1}}$. Next, we repeat the computational experiment for a sample saturated with heavy oil, using Eqns. 3.27 and 3.28 to find $\overline{\theta_v^{p_2}}$ and $\overline{\theta_d^{p_2}}$. Since we don't know how the water saturation log varies along the porosity curve, we keep a constant value for the entire depth range under consideration (Figure 3.5, blue curves). Once we calculate C_v and C_d, we can estimate effective K_{sat2}, G_{sat2} for the

entire interval of interest using Eqns. 3.31 and 3.32. Comparison of results derived from our model (Figure 3.5, green curves) with those obtained using the model developed by Ciz and Shapiro (Figure 3.5, red curves) shows that, in this situation, our model provides a better prediction of the effective bulk and shear moduli.

3.5. Chapter Summary

Using strain energy and reciprocity theory, we have derived a new approach to modeling the effective bulk and shear moduli after substitution in an isotropic composite with arbitrary pore geometry. The important points are:

Parameters $\overline{\theta_v}$ and $\overline{\theta_d}$ describe strain concentration in the pore space. They are also dependent on pore shape geometry and the nature of the pore-filling material. They can be calculated computationally or in the laboratory.

If $K_{p_1} \leq K_{p_2}$ and $G_{p_1} \leq G_{p_2}$, then $K_{sat1} \leq K_{sat2}$, $G_{sat1} \leq G_{sat2}$ and $\overline{\theta_v^{p_2}} \leq \overline{\theta_v^{p_1}}$, $\overline{\theta_d^{p_2}} \leq \overline{\theta_d^{p_1}}$ hence C_v and C_d must have non-negative values.

For any arbitrary pore shape and any pore-filling material, it is generally true that $1/\phi \geq \overline{\theta_v} > 1$ and $1/\phi \geq \overline{\theta_d} > 1$.

If volumetric and shear induced stresses are homogeneous in the pore space, then parameters $\overline{\theta_v}$ and $\overline{\theta_d}$ can be obtained using Hashin-Shtrikman bounds.

3.6. Acknowledgements

3.7. References

Andrä, H., N. Combaret, J. Dvorkin, E. Glatt, J. Han, M. Kabel, Y. Keehm, F. Krzkilla, M. Lee, C. Madonna, M. Marsh, T. Mukerji, E. H. Saenger, R. Sain, N. Saxena, S. Ricker, A. Wiegmann and X. Zhan, 2013, Digital rock physics benchmarks - Part I: Imaging and segmentation: Computers & Geosciences, **50**, 25-32.

Ciz, R., and S. A. Shapiro, 2007, Generalization of Gassmann equations for porous media saturated with a solid material: Geophysics, **72**, A75–A79.

Gassmann, F., 1951, Über die Elastizität poröser Medien: Vierteljahrschrift der Naturforschenden Gessellschaft in Zürich, **96**, 1-23.

Gibiansky, L., and S. Torquato, 1998, Rigorous connection between physical properties of porous rock: Journal of Geophysical Research, **103**, 23911-23923.

Hashin, Z., 1962, The elastic moduli of heterogeneous materials, Journal of Applied Mechanics, **29**, 143-150.

Hashin, Z., and S. Shtrikman, 1963, A variational approach to the elastic behavior of multiphase materials: Journal of the Mechanics and Physics of Solids, **11**, 127–140.

Hill, R., 1963, Elastic properties of reinforced solids: some theoretical principles: Journal of the Mechanics and Physics of Solids, **11**, 357-372.

Mavko, G., and D. Jizba, 1991, Estimating grain-scale fluid effects on velocity dispersion in rocks: Geophysics, **56**, 1940–1949.

Mavko, G. and N. Saxena, 2013, Embedded-bound method for estimating the change in bulk modulus under either fluid or solid substitution: Geophysics, **78**, 5, L87-L99.

Saxena, N., G. Mavko and T. Mukerji, 2013, Change in effective bulk modulus upon fluid or solid substitution: Geophysics, **78**, 4, L45-L56.

Wang, Z., 1988, Wave velocities in hydrocarbons and hydrocarbon saturated rocks – with applications to EOR monitoring: PhD thesis, Stanford University.

Walsh, J., 1965, The effect of cracks on the compressibility of rock: Journal of Geophysical Research, **70**, 381-389.

Chapter 4

Equations for fluid, solid, and porosity substitution

4.1. Abstract

One primary assumption of previous attempts by Gassmann (1951), Brown and Korringa (1975) and Ciz and Shapiro (2007) to develop accurate mathematical descriptions of fluid substitution is that pore geometry does not change upon substitution. In this chapter, we remove this assumption by presenting an *exact* substitution relation that takes into account both changes in fluid properties and changes in pore geometry. Our newly derived approach (Chapter 3) is applicable for modeling these scenarios. We show that for two different pore compliances of any arbitrary pore shape, the difference in volume averaged stress heterogeneity in the pore spaces remains the same. This

assumption is consistent with numerical simulations conducted on digital samples of the Fontainebleau and Berea sandstones. After presenting our results, we demonstrate the new approach using an actual data set and accompanying 3D CT-scan image.

4.2.   Introduction

The theories of Gassmann, Brown and Korringa, and Ciz and Shapiro are fundamentally limited to substitution scenarios in which pore geometry does not change. This assumption limits the applicability of the theories to problems such as modeling digenesis (Avseth et al., 2005), estimating the effects of dissolution/precipitation (Hoefiner and Le Guen et al., 2007; Vanorio et al., 2011; Vialle and Vanorio, 2011), and modeling the effect of steam injection on heavy oil reservoirs (Schmitt, 1999; Bianco et al., 2008; Chopra et al., 2010).

In this chapter we use our newly derived approach to describe solid/fluid substitution in isotropic elastic composites with arbitrary pore geometries. Our ultimate goal is to predict the changes in effective bulk and shear moduli upon substitution of any pore filling material and the change in pore compliance for any arbitrary pore shape.

4.3.   Substitution equations

Consider an initial composite K_{sat_1} , G_{sat_1} , where frame K_m, G_m with pore space ϕ_1 is fully saturated with initial pore material K_{p_1} , G_{p_1} . We can rewrite the equations derived in Chapter 3 for effective bulk and shear moduli as

$$\frac{K_m - K_{sat1}}{\phi_1\left(K_m - K_{p_1}\right)} = \overline{\theta_v^{\phi_1,p_1}} \qquad , \tag{4.1}$$

and

$$\frac{G_m - G_{sat1}}{\phi_1\left(G_m - G_{p_1}\right)} = \overline{\theta_d^{\phi_1,p_1}} \qquad . \tag{4.2}$$

Next, we consider the same composite saturated with a new pore filling material K_{p_2}, G_{p_2} and exhibiting a different pore space, ϕ_2 . We estimate new effective bulk and shear moduli as

$$\frac{K_m - K_{sat2}}{\phi_2\left(K_m - K_{p_2}\right)} = \overline{\theta_v^{\phi_2,p_2}} \qquad , \tag{4.3}$$

and

$$\frac{G_m - G_{sat2}}{\phi_2\left(G_m - G_{p_2}\right)} = \overline{\theta_d^{\phi_2,p_2}} \qquad . \tag{4.4}$$

Subtracting the equations for the final material (Eqns. 4.1 and 4.2), from those for the initial material, (Eqns. 4.3 and 4.4), we obtain

$$\frac{K_m - K_{sat_2}}{\phi_2\left(K_m - K_{p_2}\right)} - \frac{K_m - K_{sat_1}}{\phi_1\left(K_m - K_{p_1}\right)} = \overline{\theta_v^{\phi_2,p_2}} - \overline{\theta_v^{\phi_1,p_1}} \qquad , \tag{4.5}$$

and

$$\frac{G_m - G_{sat_2}}{\phi_2\left(G_m - G_{p_2}\right)} - \frac{G_m - G_{sat_1}}{\phi_1\left(G_m - G_{p_1}\right)} = \overline{\theta_d^{\phi_2,p_2}} - \overline{\theta_d^{\phi_1,p_1}} \qquad . \tag{4.6}$$

For different pore compliances, such as ϕ_1 and ϕ_2, the effective bulk and shear moduli of rocks saturated with different pore filling materials, respectively, vary.

However, if the change in pore compliance remains the same between the composites, then $\overline{\theta_v^{\phi_1,p_1}} - \overline{\theta_v^{\phi_2,p_2}}$ and $\overline{\theta_d^{\phi_1,p_1}} - \overline{\theta_d^{\phi_2,p_2}}$ are approximately constant. The assumption is supported by numerical experiments implemented on Fontainebleau and Berea sandstone digital samples.

$$\frac{K_m - K_{sat_2}}{\phi_2\left(K_m - K_{p_2}\right)} - \frac{K_m - K_{sat_1}}{\phi_1\left(K_m - K_{p_1}\right)} \approx C_v \qquad , \tag{4.7}$$

$$\frac{G_m - G_{sat_2}}{\phi_2\left(G_m - G_{p_2}\right)} - \frac{G_m - G_{sat_1}}{\phi_1\left(G_m - G_{p_1}\right)} \approx C_d \qquad , \tag{4.8}$$

If $K_{p_1} \geq K_{p_2}$, $G_{p_1} \geq G_{p_2}$ and $\phi_1 \geq \phi_2$, then $K_{sat_1} \geq K_{sat_2}$, $G_{sat_1} \geq G_{sat_2}$ and $\overline{\theta_v^{\phi_2,p_2}} \geq \overline{\theta_v^{\phi_1,p_1}}$, $\overline{\theta_d^{\phi_2,p_2}} \geq \overline{\theta_d^{\phi_1,p_1}}$; hence, C_v and C_d must have non-negative values. Subscripts *"v"* and *"d"* denote boundary conditions such as volumetric and deviatoric strain, respectively.

4.4. Application

To account for differences in volume averaged stress heterogeneity in the two pore spaces, we need information about pore geometry such as porosity, volume fraction, or a CT scan image. Parameters $\overline{\theta_v}$ and $\overline{\theta_d}$ can be estimated computationally using a 3D CT-scan image or experimentally using laboratory measurements for *Vp* and *Vs* in a core sample. $\overline{\theta_v}$ and $\overline{\theta_d}$ depend on the pore geometry and pore filling material. As a result, for computational and laboratory experiments it is necessary to estimate these parameters for a composite saturated with the final pore filling material and corresponding geometry. In

computational simulations, parameters $\overline{\theta_v}$ and $\overline{\theta_d}$ can be obtained directly or by using

Eqns. 4.3 and 4.4 from K_{sat2} and G_{sat2}. These parameters can be also approximated

using $\overline{\theta_v}$ and $\overline{\theta_d}$ bounds.

To test the application of our results, we refer to well log data and a corresponding

3D CT-scan image (Figure 4.1a) from a reservoir saturated with heavy oil. The CT-scan

image (Figure 4.1a) shows that, for this particular reservoir, the quartz grains (blue color)

are somewhat suspended in heavy oil (white color). If we were to replace the heavy oil

(bulk modulus: 3.2 GPa, shear modulus: 0.4 GPa) with a fluid such as water (bulk

modulus: 2.2 GPa, shear modulus: 1 Pa), the suspended grains would no longer have the

support of a solid pore filling material; this causes compaction and an increase in the

number of contacts per grain. As a result, pore compliance changes as well as the volume

fraction of the pore space.

In order to evaluate our main assumption, we modify the original 3D CT-scan image

(Figure 4.1a) by numerically adding a few voxels around each grain, thereby increasing

the number of contacts per grain and reducing the volume fraction of pore space (Figure

4.1b).
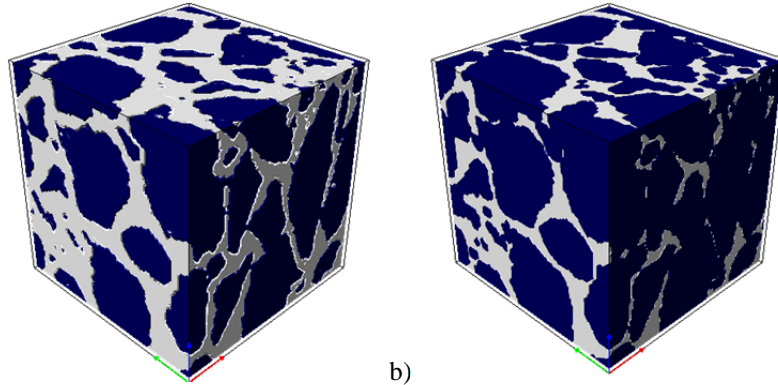
a)   b)

Figure 4.1: 3D CT-scan image of a sample containing quartz grains (blue, bulk modulus: 37 GPa, shear modulus: 44 GPa). a) Original image filled with heavy oil (white, bulk modulus: 3.2 GPa, shear modulus: 0.4 GPa) and b) numerically altered image filled with water (white, bulk modulus: 2.2 GPa, shear modulus: 1 Pa)

Next, we numerically estimate the porosity ($\phi_2 = 0.27$) of the altered sample and fill the pore space with water, assuming that grains are pure quartz. After applying volumetric and deviatoric boundary conditions, we calculate the effective bulk (K_{sat2}) and shear (G_{sat2}) moduli. Using Eqns. 4.3 and 4.4, we estimate exact values for strain concentration in the pore space, $\overline{\theta_v^{\phi_2 water}}$ and $\overline{\theta_d^{\phi_2 water}}$. We repeat the same numerical experiment with the original 3D image of porosity (with $\phi_1 = 0.36$ and a pore space filled with heavy oil), finding K_{sat_1}, G_{sat_1} and $\overline{\theta_v^{\phi_1 heavyoil}}$, $\overline{\theta_d^{\phi_1 heavyoil}}$. To determine how K_{sat2} and G_{sat2} vary throughout the entire range of porosity, we subtract the difference between ϕ_1 and ϕ_2 of numerically estimated 3D images and from the original porosity measured in the well log (Figure 4.3, black curve on porosity). In Figure 4.3, the result for new porosity is displayed as a blue curve. Using this curve, we estimate effective bulk K_{sat2} and shear G_{sat2} moduli for a rock fully saturated with water, assuming that

$\overline{\theta_v^{\phi_2 water}}$ and $\overline{\theta_d^{\phi_2 water}}$ do not change with the porosity (Eqns. 4.3 and 4.4). K_{sat2} and G_{sat2} are displayed in Figure 4.3 as blue curves. In Figure 4.2, the effective bulk and shear moduli of water saturated and original well log data are also plotted along with Hashin-Shtrikman bounds. The variation in effective bulk and shear moduli in rocks fully saturated with water is very large.

Assume now that we do not have the water saturated effective bulk and shear moduli. We will predict the effective elastic properties of a fully water saturated compacted frame using the new porosity (blue porosity curve on Figure 4.3). We find $\overline{\theta_v^{water}} - \overline{\theta_v^{heavyoil}}$ and $\overline{\theta_d^{water}} - \overline{\theta_d^{heavyoil}}$, assuming that C_v and C_d are approximately constant values. Now, using approximate values of C_v and C_d in Eqns. 4.7 and 4.8, we can solve for effective bulk K_{sat2}^{water} and shear G_{sat2}^{water} moduli with corresponding porosity ϕ_2. The calculated effective elastic properties are plotted in red (Figures 4.2 and 4.3). These curves fall in the range of the numerically comptuted effective bulk and shear moduli (blues color curves), but display less variation with depth.
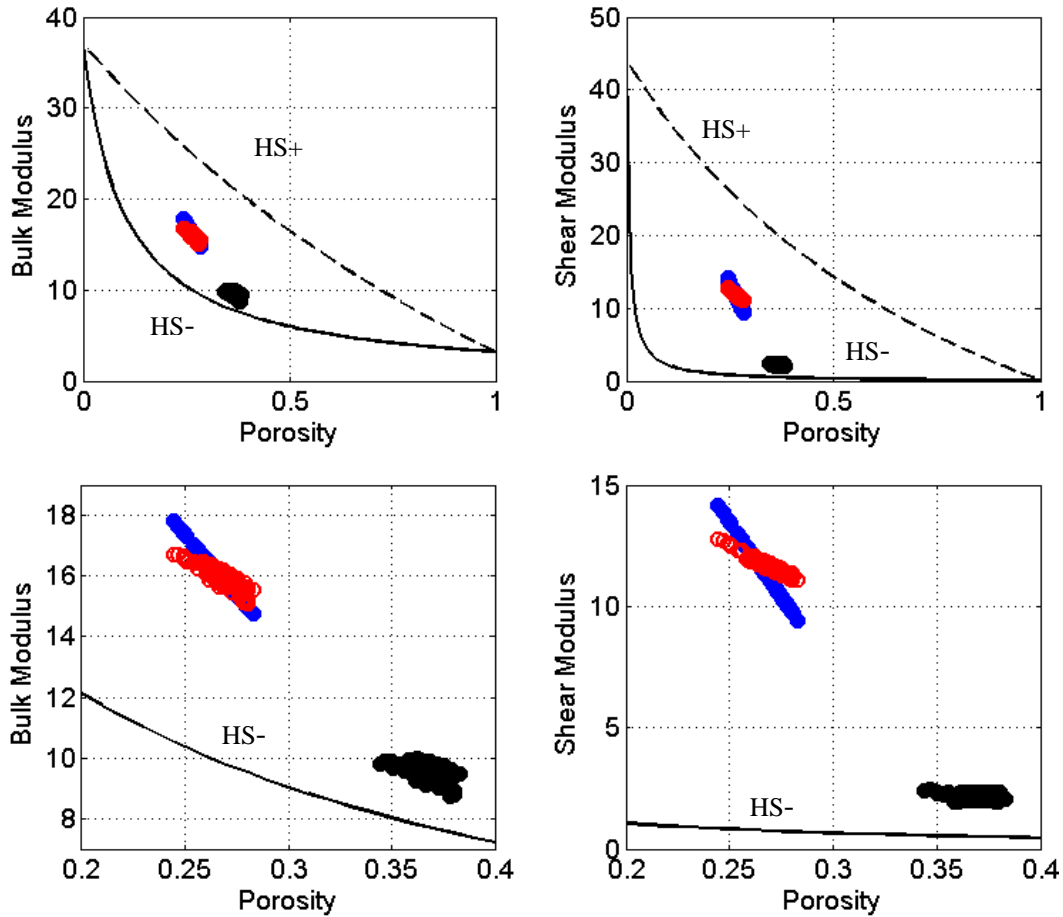
Figure 4.2: *Top row:* Effective bulk and shear moduli. *Bottom row:* The same plot focused on the area of interest. The black circles represent well log data for a pure sandstone saturated with heavy oil. Blue circles represent numerically estimated effective elastic properties from an altered 3D CT scan image of a sandstone sample fully saturated with water. Red circles represent samples where heavy oil was replaced with water using Eqns. 4.7 and 4.8.
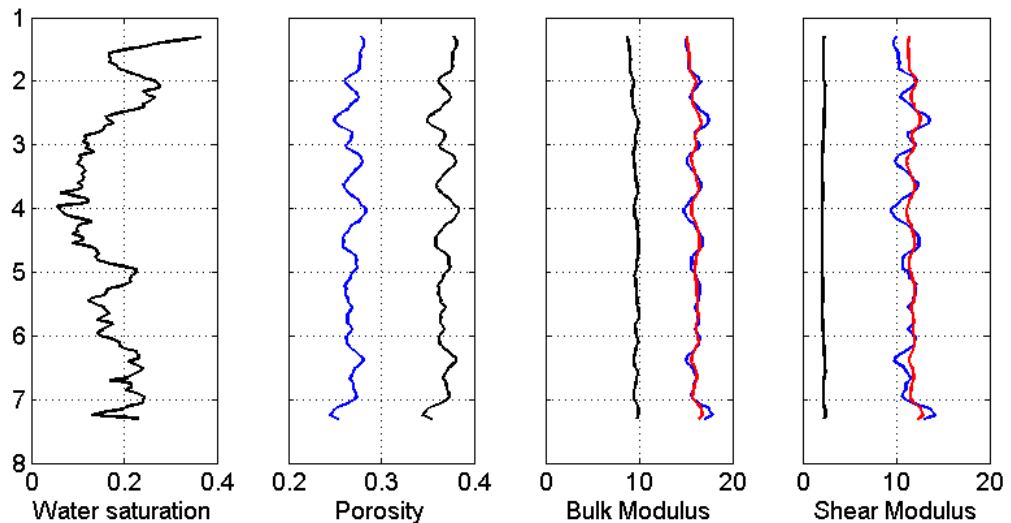
Figure 4.3: Model results vs well log data: Black curves show original well log data for an interval saturated with heavy oil (bulk: 3.2 GPa and shear: 0.1 GPa). Blue curves show the altered porosity, effective bulk and shear moduli numerically computed from a CT-scan image fully virtually saturated with water (bulk: 2.2 GPa and shear: 1Pa). Red curves show the predicted bulk and shear moduli of rock fully saturated with water using Eqns. 4.7 and 4.8.

4.5. Chapter summary

Our exact equations can be approximated for predicting the change in effective bulk and shear modulus upon substitution of *any* pore filling material and change in pore compliance for *any* arbitrary pore shape. Eqns. 4.7 and 4.8 are the primary results of this chapter. They allow for the modeling of substitution accompanied by changes in pore geometry. However, they do require knowledge of the final pore geometry. From Chapter 3 we already know these important points:

Parameters $\overline{\theta_v}$ and $\overline{\theta_d}$ describe strain concentration in the pore space. They are also dependent on pore shape geometry and the nature of the pore-filling material. They can be calculated computationally or in the laboratory.

If $K_{p_1} \geq K_{p_2}$, $G_{p_1} \geq G_{p_2}$ and $\phi_1 \geq \phi_2$, then $K_{sat_1} \geq K_{sat_2}$, $G_{sat_1} \geq G_{sat_2}$ and

$\overline{\theta_v^{\phi_2, P_2}} \geq \overline{\theta_v^{\phi_1, P_1}}$, $\overline{\theta_d^{\phi_2, P_2}} \geq \overline{\theta_d^{\phi_1, P_1}}$; hence, C_v and C_d must have non-negative values.

For any arbitrary pore shape and any pore-filling material, it is generally true that

$1/\phi \geq \overline{\theta_v} > 1$ and $1/\phi \geq \overline{\theta_d} > 1$.

If volumetric and shear induced stresses are homogeneous in the pore space, then

parameters $\overline{\theta_v}$ and $\overline{\theta_d}$ can be obtained using Hashin-Shtrikman bounds.

4.6.   Acknowledgements

4.7.   References

Andrä, H., N. Combaret, J. Dvorkin, E. Glatt, J. Han, M. Kabel, Y. Keehm, F. Krzikalla, M. Lee, C. Madonna, M. Marsh, T. Mukerji, E. H. Saenger, R. Sain, N. Saxena, S. Ricker, A. Wiegmann and X. Zhan, 2013, Digital rock physics benchmarks - Part I: Imaging and segmentation: Computers & Geosciences, **50**, 25-32.

Bachrach, R., J. Dvorkin, A. Nur., 1998, High-resolution shallow-seismic experiments in sand, Part II: Velocities in shallow unconsolidated sand: Geophysics, **63** (4), 1234-1240.

Berryman, J. G., 1980, Long-wavelength propagation in composite elastic media: Journal of the Acoustical Society of America, **68**, 1809–1831.

Berryman, J. G. , 1999, Origin of Gassmann's equations: Geophysics, **64**, 1627–1629.

Castagna, J. P., M. L. Batzle, and T. K. Kan, 1993, Rock physics: the link between rock properties and AVO response: in J. P. Castagna and M. M. Backus, Eds., Offset -

Dependent Reflectivity - Theory and Practice of AVO Analysis, Society of Exploration Geophysicists.

Cleary, M. P., I. W. Chen and S. M. Lee, 1980, Self-consistent techniques for heterogeneous media: ASCE Journal of Engineering Mechanics, **106**, 861-887.

Dvorkin, J., G. Mavko, and B. Gurevich, 2007, Fluid substitution in shaley sediment using effective porosity: Geophysics, 72 (3), O1-O8.

Eshelby, J. D., 1957, The determination of the elastic field of an ellipsoidal inclusion, and related problems: Proceedings of Royal Society London, A, 241, 376-396.

Gassmann, F., 1951, Über die Elastizität poröser Medien: Vierteljahrschrift der Naturforschenden Gessellschaft in Zürich, **96**, 1-23.

Greenberg, M.L., and J. P. Castagna, 1992, Shear-wave velocity estimtaion in porous rocks: theoretical formulation, preliminary verification and applications: Geophysical Prospecting, **40**, 195-209.

Han, G, 1986, Effects of porosity and clay content on acoustic properties of sandstones and unconsolidated sediments, PhD dissertation, Stanford University.

Han, G., and M. Batzle, 2004, Gassmann's equation and fluid-saturation effects on seismic velocities: Geophysics, **69**, 2, 398-405.

Kuster, G. T., and M. N. Toksöz, 1974, Velocity and attenuation of seismic waves in two phase media: Part I. theoretical formulations: Geophysics, **39**, 587-606.

Sengupta, M., G. Mavko, and T. Mukerji, 2003, Quantifying subresolution saturation scales from time-lapse seismic data: A reservoir monitoring case study: Geophysics, **68**:3, 803-814.

Mavko, G., C. Chan, and T. Mukerji, 1995, Fluid substitution: Estimating changes in Vp without knowing Vs: Geophysics, **60**, 1750–1755.

Mavko, G., T. Mukerji and J. Dvorkin, 2009, The Rock Physics Handbook: Cambridge University Press.

Norris, A. N., 1985, A differential scheme for the effective moduli of composites: Mechanics of Materials, **4**, 1-16.

O'Connell, R. J., B. Budiansky, 1974, Seismic velocities in dry and saturated cracked solids: Journal of Geophysical Research, **79**, 5412–5426.

Røgen, B., L. Gommesen, L. Fabricius, 2004, Methods of velocity prediction tested for North Sea chalk: a review of fluid substitution and Vs estimates: Journal of Petroleum Science and Engineering, **45**:1-2, 129-139.

Saxena, N., and G. Mavko, 2014, Exact equations for fluid and solid substitution: Geophysics, **79**, 3, L21-L32.

Torquato, S., 2001, Random heterogeneous materials: Microstructure and macroscopic properties: Springer.

Yan, F., and D. Han, 2010, Some consideration about fluid substitution without shear wave velocity: SEG Technical Program Expanded Abstracts, 2741-2745.

Vanorio, T., C. Scotallero, and G. Mavko, 2008, The effect of chemical and physical processes on the acoustic properties of carbonate rocks: The Leading Edge, **27**, 1040–1048.

Vernik, L., D. Fisher and S. Bahret, 2002, Estimation of net-to-gross from P and S impedance in deepwater turbidities: The Leading Edge, **21**, 380-387.

Wu, T. T., 1966, The effect of inclusion shape on the elastic moduli of a two-phase material: International Journal of Solids and Structures, **2**, 1-8.

Chapter 5

Approximation for strain concentration tensors for fluid and solid substitution

5.1. Abstract

In this chapter we continue to develop a method for modeling solid substitution in an elastic isotropic composite using strain concentration tensors. In our previous study, we showed that the new approach is exact if we have information about pore geometry such as 3D CT-scan image, laboratory measurements or well log data. In the paper we introduce an approximation for use in cases where such information is unavailable. After discussing new insights into strain concentration tensors, we show how our new approximation can narrow a range of possible solution upon substitution.

5.2. Introduction

In previous papers we discussed a new approach to modeling fluid-to-solid substitution for an elastic isotropic composite for any pore-filling material. Our ultimate goal was to reduce the amount of computational estimation required and develop an alternative method for quantifying stress heterogeneity in the pore space. The previously published method provided a smaller range of solutions for pore compliance parameters:

$$\frac{K_m - K}{\phi(K_m - K_p)} = \overline{\theta_v} \qquad ; \tag{5.1}$$

$$\frac{G_m - G}{\phi(G_m - G_p)} = \overline{\theta_d} \qquad . \tag{5.2}$$

Parameter $\overline{\theta_v}$ is the volumetric strain concentration in the pore space, defined as the average strain in the pore space divided by the average strain in the rock. Parameter $\overline{\theta_v}$ is the ratio of volume strain of the pore space to volume strain of the entire rock. Parameter $\overline{\theta_d}$, introduced in Eqn. 5.2, captures the concentration strain of induced shear stress in the pore space. For any arbitrary pore shape, a general argument can be made that $1/\phi \geq \overline{\theta_v} > 1$ and $1/\phi \geq \overline{\theta_d} > 1$. Parameters $\overline{\theta_v}$ and $\overline{\theta_d}$ depend on the pore space geometry and the properties of the pore-filling material. In Eqns. 5.1 and 5.2, ϕ is the porosity, K_p and G_p are the bulk and shear moduli of the pore-filling material, K_m and G_m are the bulk and shear moduli of the mineral in the rock frame, and K and G are the effective bulk and

shear moduli of the composite. In this paper, subscripts *"v"* and *"d"* denote the boundary conditions of volumetric and deviatoric strain, respectively.

Consider an initial composite K_{sat}, G_{sat}, where frame K_m, G_m with pore space ϕ is fully saturated with initial pore material K_{p_1}, G_{p_1}. We can write Eqn. 5.1 and 5.2 as

$$\frac{K_m - K_{sat1}}{\phi\left(K_m - K_{p_1}\right)} = \overline{\theta_v^{p_1}} \qquad , \qquad (5.3)$$

and

$$\frac{G_m - G_{sat1}}{\phi\left(G_m - G_{p_1}\right)} = \overline{\theta_d^{p_1}} \qquad . \qquad (5.4)$$

Next, we consider same composite saturated with a new pore filling material K_{p_2}, G_{p_2} and estimate the new effective bulk and shear moduli:

$$\frac{K_m - K_{sat2}}{\phi\left(K_m - K_{p_2}\right)} = \overline{\theta_v^{p_2}} \qquad , \qquad (5.5)$$

and

$$\frac{G_m - G_{sat2}}{\phi\left(G_m - G_{p_2}\right)} = \overline{\theta_d^{p_2}} \qquad . \qquad (5.6)$$

Subtracting the equations for the final material, (5.5) and (5.6), from those for the initial material, (5.3) and (5.4), we obtain

$$\frac{K_m - K_{sat1}}{\phi(K_m - K_{P_1})} - \frac{K_m - K_{sat2}}{\phi(K_m - K_{P_2})} = \overline{\theta_v^{p_1}} - \overline{\theta_v^{p_2}} \qquad , \tag{5.7}$$

and

$$\frac{G_m - G_{sat1}}{\phi(G_m - G_{P_1})} - \frac{G_m - G_{sat2}}{\phi(G_m - G_{P_2})} = \overline{\theta_d^{p_1}} - \overline{\theta_d^{p_2}} \qquad . \tag{5.8}$$

We will consider $\overline{\theta_v^{p_1}} - \overline{\theta_v^{p_2}}$ and $\overline{\theta_d^{p_1}} - \overline{\theta_d^{p_2}}$ as measures of pore compliance. If porosity changes, the effective bulk and shear moduli may also change; however, if porosity changes within the same pore compliance, then $\overline{\theta_v^{p_1}} - \overline{\theta_v^{p_2}}$ and $\overline{\theta_d^{p_1}} - \overline{\theta_d^{p_2}}$ are approximately constant:

$$\frac{K_m - K_{sat1}}{\phi(K_m - K_{P_1})} - \frac{K_m - K_{sat2}}{\phi(K_m - K_{P_2})} \approx C_v \qquad , \tag{5.9}$$

$$\frac{G_m - G_{sat1}}{\phi(G_m - G_{P_1})} - \frac{G_m - G_{sat2}}{\phi(G_m - G_{P_2})} \approx C_d \qquad . \tag{5.10}$$

If $K_{P_1} \leq K_{P_2}$ and $G_{P_1} \leq G_{P_2}$, then $K_{sat_1} \leq K_{sat_2}$, $G_{sat_1} \leq G_{sat_2}$ and $\overline{\theta_v^{p_2}} \leq \overline{\theta_v^{p_1}}$, $\overline{\theta_d^{p_2}} \leq \overline{\theta_d^{p_1}}$; hence, C_v and C_d must have non-negative values. In this paper, subscripts *"v"* and *"d"* denote boundary conditions of volumetric and deviatoric strain, respectively.

5.3.   Bounds for strain concentration tensor

5.3.1. Volumetric strain concentration tensor

Using Eshelby's theory, the volumetric strain concentration in the pore space can be expressed using the averaged volumetric strain in the pore space $\varepsilon^p{}_{kk}$ and the averaged effective volumetric strain of the entire sample ε_{kk} :

$$\overline{\theta}_v = \frac{\varepsilon^p{}_{kk}}{\varepsilon_{kk}} \quad , \tag{5.11}$$

where ε_{kk} is the exact relation of the *change* in the volume ΔV of the effective composite to the initial volume V of the effective composite:

$$\varepsilon_{kk} = \frac{\Delta V}{V} \quad . \tag{5.12}$$

This relation can be rewritten for the volumetric strain in the pore space $\varepsilon^p{}_{kk}$ as the ratio of the *change* in the pore volume ΔV^p of the effective composite to the total pore volume V^p of the effective composite, where the total pore volume is $V^p = \phi V$:

$$\varepsilon^p_{kk} = \frac{\Delta V^p}{V^p} = \frac{\Delta V^p}{\phi V} \quad . \tag{5.13}$$

Substituting the terms from Eqns. 5.12 and 5.13 in Eqn. 5.11, we get

$$\overline{\theta}_v = \frac{1}{\phi} \frac{\Delta V^p}{\Delta V} \quad . \tag{5.14}$$

The *volumetric* strain concentration tensor can now be described as the ratio between volume changes in the pore space to the volume change of the total composite:

$$\overline{\theta}_v = \frac{\Delta\phi_v}{\phi} \qquad .$$

(5.15)

We can rewrite Eqns. 5.11 as

$$\frac{K_m - K}{K_m - K_p} = \Delta\phi_v \qquad .$$

(16)

5.3.2. Deviatoric strain concentration tensor

Using Eshelby's theory, strain concentration in the pore space can be expressed using the averaged deviatoric strain in the pore space ε_d^p and the averaged deviatoric strain of the entire sample ε_d :

$$\overline{\theta}_d = \frac{\varepsilon_d^p}{\varepsilon_d} \qquad ,$$

(5.17)

where ε_{xy} is the exact relation of the *change* in the pore space in the direction of applied simple share ΔD of the effective composite to the initial volume V of the effective composite for the *simple shear* boundary conditions:

$$\varepsilon_d = \frac{\Delta D}{V} \qquad .$$

(5.18)

This relation can be rewritten for the deviatoric strain in the pore space ε_d^p as the ratio of the *change* in the pore space ΔD^p of the effective composite to the total pore volume V^p of the effective composite, where the total pore volume is $V^p = \phi V$:

$$\varepsilon_d^p = \frac{\Delta D^p}{V^p} = \frac{\Delta D^p}{\phi V} \qquad .$$
(5.19)

Substituting the terms from Eqns. 5.18 and 5.19 in Eqn. 5.17, we get

$$\overline{\theta_d} = \frac{1}{\phi} \frac{\Delta D^p}{\Delta D} \qquad .$$
(5.20)

The *deviatoric* strain concentration tensor can now be described as the ratio of deviatoric changes in the pore space to the volume change of total composite:

$$\overline{\theta_d} = \frac{\Delta \phi_d}{\phi} \qquad .$$
(5.21)

We can rewrite Eqns. 5.21 as

$$\frac{G_m - G}{G_m - G_p} = \Delta \phi_d \qquad .$$
(5.22)
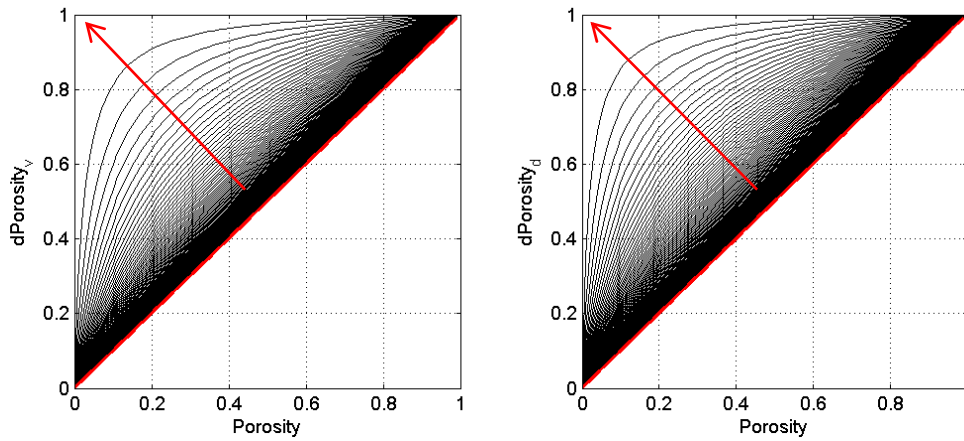
Figure 5.1: 2D illustration of HS bounds representation (left) and a slice view of the Berea sandstone (right).

5.3.3. Strain concentration tensor bounds

Eqns. 5.16 and 5.22 contain two sets of *unknown* values: the effective bulk and shear moduli and the change in the pore space with volumetric and deviatoric boundary conditions. Computational simulations must be used to exactly estimate parameters $\Delta\phi_v$ and $\Delta\phi_d$. However, we have found that, using Hashin-Shtrikman (HS) bounds, it is possible to narrow down the range of possible solutions for effective bulk and shear modulus upon solid substitution. Hashin-Shtrikman (HS) bounds allow us to adjust porosity according to the effective bulk and shear moduli. This means that we can always find exact values for effective elastic properties that match with lower and upper HS bounds by adjusting porosity values.

Consider an initial composite where frame K_m, G_m with pore space ϕ is fully saturated with initial pore material $K_p^{(1)}$, $G_p^{(1)}$. Using HS bounds, we can calculate effective bulk $K_{(1)}^{(\pm)}$ and shear moduli $G_{(1)}^{(\pm)}$. From Eqns. 5.1 and 5.2 we can calculate volumetric $\overline{\theta_{v(1)}^{\pm}}$ and deviatoric strain concentration tensors $\overline{\theta_{d(1)}^{\pm}}$ as:

$$\frac{K_m - K_{(1)}^{\pm}}{\phi\left(K_m - K_p^{(1)}\right)} = \overline{\theta_{v(1)}^{\pm}} \qquad , \qquad (5.23)$$

and

$$\frac{G_m - G_{(1)}^{\pm}}{\phi\left(G_m - G_p^{(1)}\right)} = \overline{\theta_{d(1)}^{\pm}} \qquad , \qquad (5.24)$$

Since the actual effective elastic properties of the initial composite are known, we can estimate actual $\Delta\phi_v$ and $\Delta\phi_d$ using Eqns. 5.16 and 5.22. We can now adjust the fitting volumetric $\gamma_v^{\pm}$ and deviatoric porosity $\gamma_d^{\pm}$ using Eqns. 5.15 and 5.21 and volumetric $\overline{\theta_{v(1)}^{\pm}}$ and deviatoric strain concentration tensors $\overline{\theta_{d(1)}^{\pm}}$:

$$\gamma_v^{\pm} = \frac{\Delta\phi_v}{\overline{\theta_{v(1)}^{\pm}}} \qquad , \qquad (5.25)$$

and

$$\gamma_d^{\pm} = \frac{\Delta\phi_d}{\overline{\theta_{d(1)}^{\pm}}} \qquad . \qquad (5.26)$$

Replacing initial pore material $K_p^{(1)}$, $G_p^{(1)}$ with final pore material $K_p^{(2)}$, $G_p^{(2)}$ and HS

effective bulk $K_{(2)}^{(\pm)}$ and shear moduli $G_{(2)}^{(\pm)}$ in Eqns. 5.1 and 5.2, we estimate volumetric

$\overline{\theta_{v(2)}^{\pm}}$ and deviatoric $\overline{\theta_{d(2)}^{\pm}}$ strain concentration tensors. Next, using Eqns. 5.15 and 5.21,

we can estimate the volumetric and deviatoric change in the pore space filled with the

final pore filling material:

$$\Delta\gamma_v^{\pm} = \gamma_v^{\pm}\overline{\theta_{v(2)}^{\pm}} \qquad , \qquad (5.26)$$

and

$$\Delta\gamma_d^{\pm} = \gamma_d^{\pm}\overline{\theta_{d(2)}^{\pm}} \qquad . \qquad (5.27)$$

Even if no additional information about pore shape is available, we can always refer

to the HS bounds. Eqns. 5.23 and 5.24 describe how *fitting* porosity values $\Delta\gamma_v^{\pm}$ and $\Delta\gamma_d^{\pm}$

can be estimated using HS bounds:

$$\frac{K_m - K_{(2)}^{\pm}}{K_m - K_{(1)}^{\pm}}\frac{K_m - K_p^{(1)}}{K_m - K_p^{(2)}} = \frac{\Delta\gamma_v^{\pm}}{\Delta\phi_v} \qquad , \qquad (5.28)$$

and

$$\frac{G_m - G_{(2)}^{\pm}}{G_m - G_{(1)}^{\pm}}\frac{G_m - G_p^{(1)}}{G_m - G_p^{(2)}} = \frac{\Delta\gamma_d^{\pm}}{\Delta\phi_d} \qquad , \qquad (5.29)$$

where $K_p^{(1)}$ and $K_p^{(2)}$ are bulk moduli of the initial and final pore filling material,

$G_p^{(1)}$ and $G_p^{(2)}$ are the shear moduli of the initial and final pore filling material, and $\Delta\phi_v$

and $\Delta\phi_d$ are the volumetric and deviatoric pore space changes of the initial pore filling

material. $K_{(1)}^{\pm}$ and $K_{(2)}^{\pm}$ are the effective HS bulk moduli of the initial and final pore

filling material, and $G_{(1)}^{\pm}$ and $G_{(2)}^{\pm}$ are the effective HS shear moduli of the initial and

final pore filling materials.

We can now rewrite Eqns. 5.16 and 5.22 using $\Delta\gamma_v^{\pm}$ and $\Delta\gamma_d^{\pm}$ for the final pore filling

material and estimate the range of possible effective elastic properties:

$$\frac{K_m - K_{(2)}}{K_m - K_p^{(2)}} = \Delta\gamma_v^{\pm} \qquad , \qquad (5.30)$$

and

$$\frac{G_m - G_{(2)}}{G_m - G_p^{(2)}} = \Delta\gamma_d^{\pm} \qquad . \qquad (5.31)$$

5.3.4. Discussion

An example of this approach is shown in Figure 5.2 and 5.3. The HS bounds (red

color curves) denote a much wider range than the range determined using the new

approach (black color curves). In both cases, the actual numerical values fall between the

new bounds (blue color curves). The numerical values are from a sample saturated with

the solid pore filling material. Our new approach can successfully be used to predict

effective bulk and shear moduli for a rock frame upon substitution of a solid pore-filling

material for a fluid pore-filling material.
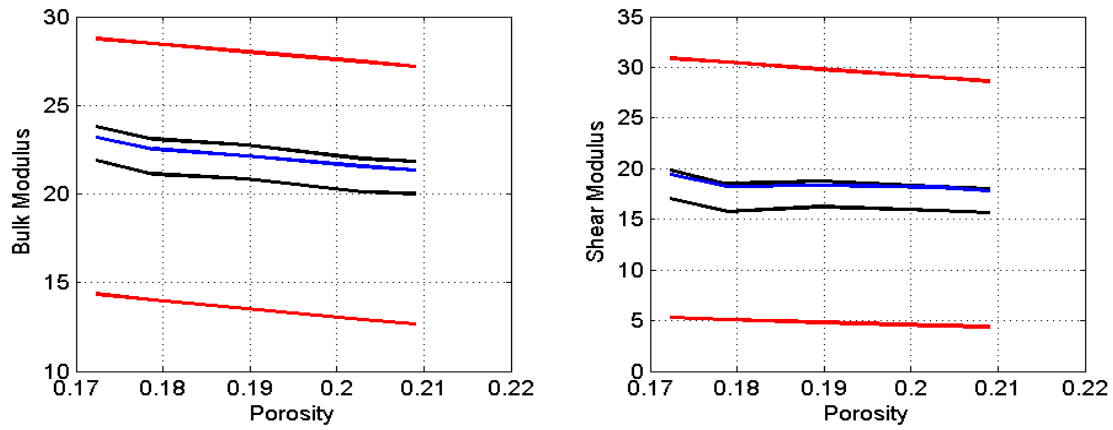
Figure 5.2: Results calculated using Eqns. 5.9 and 5.10 are shown as black curves. HS bounds are shown as red curves. The blue curve shows actual numerical values computed using 5 Berea subsamples filled with solid material.
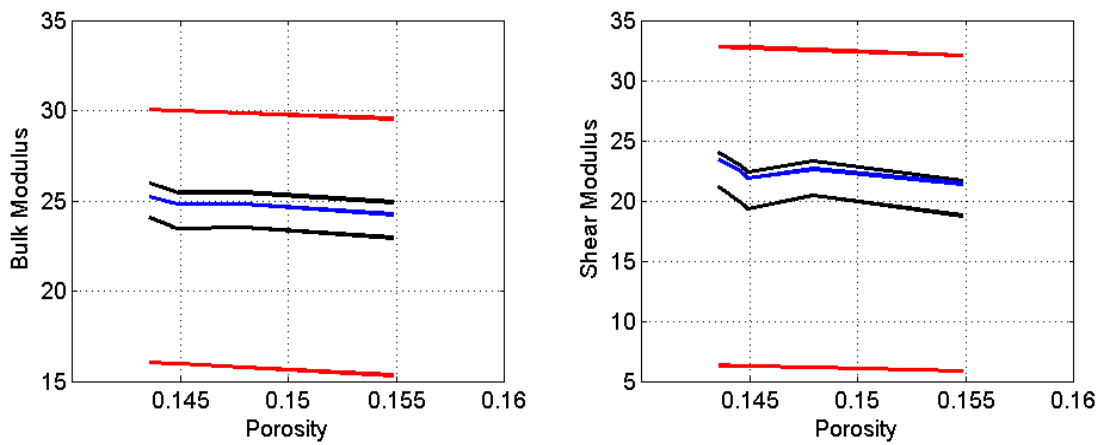
Figure 5.3: Results calculated using Eqns. 5.9 and 5.10 are shown as black curves. HS bounds are shown as red curves. The blue curve shows actual numerical values computed using 5 Fontainebleau subsamples filled with solid material.

5.4. Application

5.4.1. Digital samples
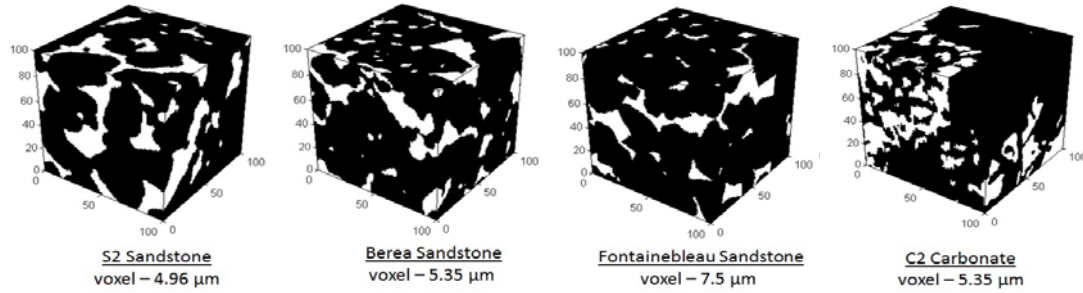
Figure 5.4: Digital samples of rocks used in computational simulations

To study an application of our new method we refer to three sandstone samples: S2, Berea, and Fontainebleau sandstone, and one carbonate sample: C2 (Figure 5.4). The size of each of these 3D CT scan images is approximately 300^3, which is too large to run computational simulations on. Hence, we divide each 3D CT scan cube into 100^3 sub-cubes and randomly choose 5 sub-samples. The material properties used in our calculations are shown in Table 5.1.

Table 5.1: Phase properties taken from Mavko et al. (2009).

Mineral	Bulk modulus (GPa)	Shear modulus (GPa)	Density (g/cc)
Quartz	37	44	2.65
Calcite	77	32	2.71
Water	2.2	0	1
Cold heavy oil (Behura et al., 2007)	3.2	0.5	-
Kerogen (Vernik and Liu, 1997)	5.5	3.2	-
Gas	0	0	0.1

5.4.2. Sandstones

On the Figure 5.5 we show 5 sub-samples of Berea sandstone saturated with cold heavy oil in black color points and saturated with air in blue color points. The black color solid curves show the result of solid substitution of air saturated sub-samples with cold heavy oil. We observe that the actual computational simulations of the sub-samples of Berea sandstone with pore filling material as cold heavy oil are bounded between the range of possible solutions. The upper range suggests the *maximum* change in effective moduli, which implies the large strain heterogeneity in the pore space; whereas the lower range is the *minimum* change in effective moduli, which implies the strain homogeneity in the pore space.

Figure 5.5: Berea sandstone: Black dashed curves are HS bounds saturated with heavy oil. Black solid curves show the lower limits of the effective bulk and shear moduli as estimated using Eqns. 5.3 and 5.4. Blue color points are Berea sandstone saturated with air. Black color points are Berea sandstone saturated with cold heavy oil.

We repeat the same experiment with Fontainebleau and S2 sandstones and show the results on Figure 5.6 and 5.7, respectively. We substitute air pore filling material in 5 sub-samples of sandstone (blue color points) with cold heavy oil pore filling material (black color points). We observe that the actual computational simulations of the 5 sub-samples of Fontainebleau and S2 sandstones are bounded between the ranges of possible solutions, which are shown in solid black curves. The upper range suggests the *maximum* change in pore material and also implies the strain heterogeneity in the pore space, whereas the lower range is the *minimum* change in pore material and implies the stain homogeneity in the pore space.
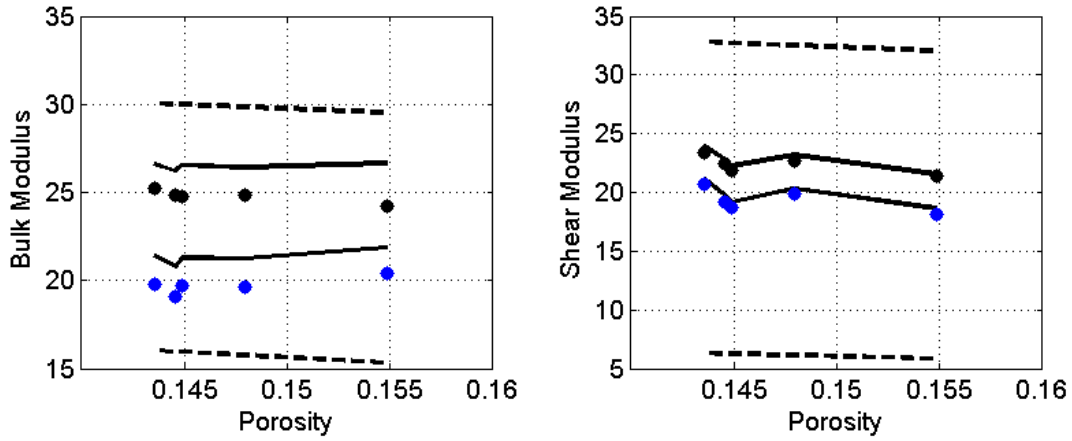
Figure 5.6: Fontainebleau sandstone: Black dashed curves are HS bounds saturated with heavy oil. Black solid curves show the lower limits of the effective bulk and shear moduli as estimated using Eqns. 5.3 and 5.4. Blue color points are Fontainebleau sandstone saturated with air. Black color points are Fontainebleau sandstone saturated with cold heavy oil.
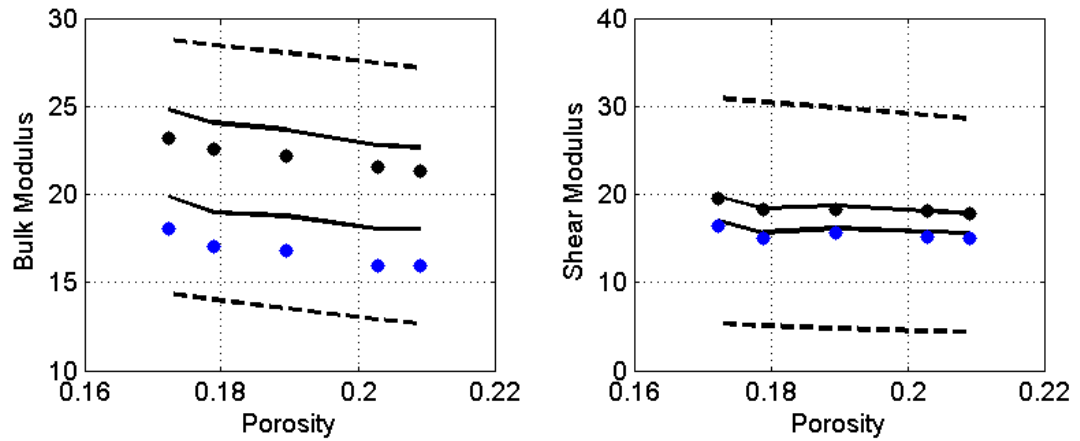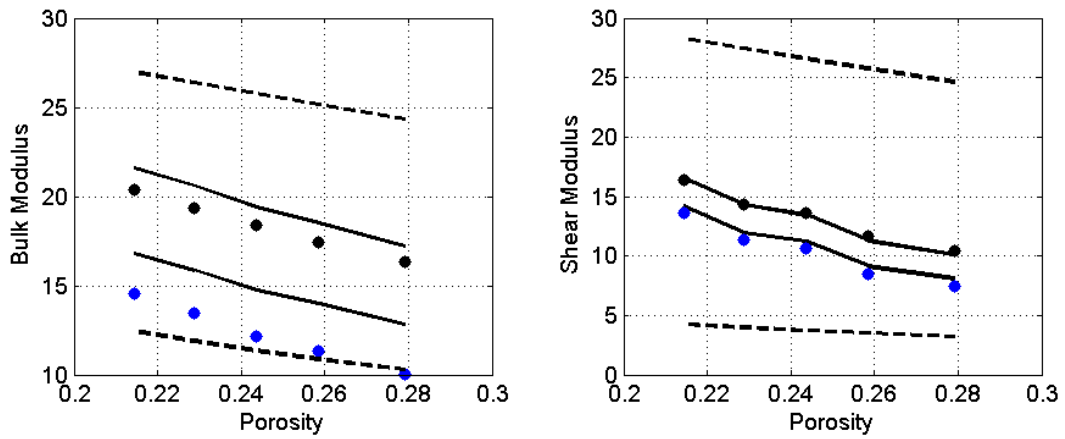

Figure 5.7: S2 sandstone: Black dashed curves are HS bounds saturated with heavy oil. Black solid curves show the lower limits of the effective bulk and shear moduli as estimated using Eqns. 5.3 and 5.4. Blue color points are S2 sandstone saturated with air. Black color points are S2 sandstone saturated with cold heavy oil.

5.4.3. Carbonates

On the Figure 5.8 we show 5 sub-samples of C2 carbonate saturated with kerogen in black color points and air in blue color points. The blue color solid curves show the result of substitution of kerogen saturated 5 sub-samples with air. We observe that the actual computational simulations of 5 sub-samples of C2 carbonate with pore filling material as air are bounded between the range of possible solutions. Then, the upper range suggests the *minimum* change in pore material and also implies the strain heterogeneity in the pore space, whereas the lower range is the *maximum* change in pore material and implies the strain homogeneity in the pore space.
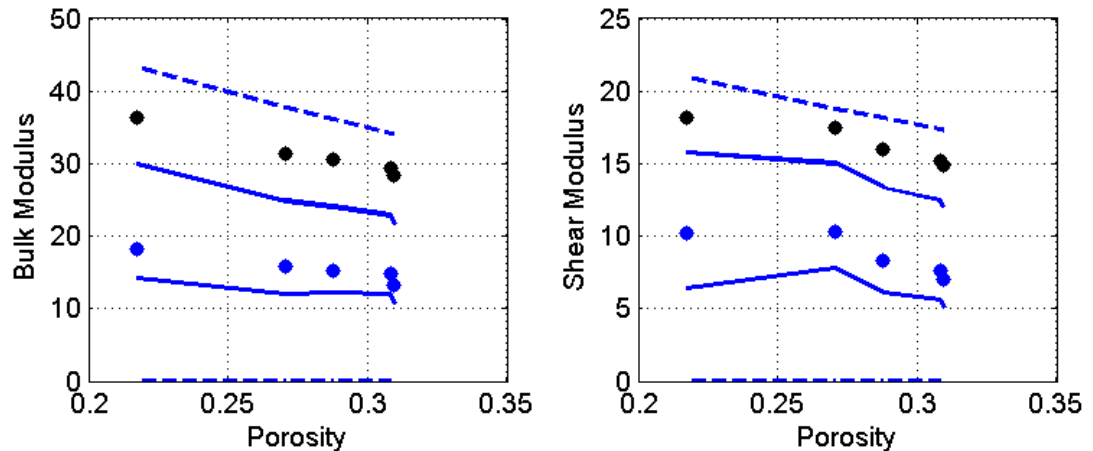
Figure 5.8: C2 carbonate: Blue dashed curves are HS bounds saturated with air. Blue solid curves show the lower limits of the effective bulk and shear moduli saturated with air and estimated using Eqns. 5.3 and 5.4. Blue color points are C2 carbonate saturated with air. Black color points are C2 carbonate saturated with kerogen.

5.4.4. Well log data

Our new method can be also applied to well log data. On Figure 5.9 we show well log data, the pore space of which is saturated with heavy oil (Bulk modulus: 3.0 GPa, Shear

modulus: 0.1 GPa), in black color points. The blue color points show the result of

substitution of heavy oil saturated well log with water. We cannot conclude whether our

range is a good approximation due to lack of actual well log data saturated with water.

However, we can guess that the data might fall somewhere close to the maximum change

in pore filling material, which is the lower range of possible solutions. As a result of our

new method we also show a range of possible solutions saturated with water in blue color

curves on Figure 5.11.
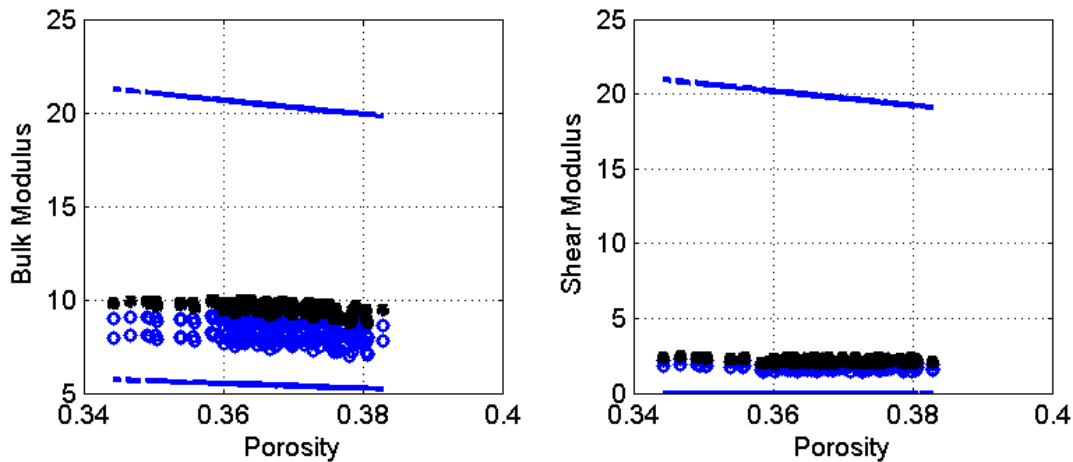
Figure 5.9: Cenovus well log data: Blue curves are HS bounds saturated with water. Blue points show the lower limits of the effective bulk and shear moduli saturated with water and estimated using Eqns. 5.3 and 5.4. Black color points are the actual well log data saturated with oil sand (Bulk modulus: 3.0 GPa, Shear modulus: 0.1 GPa)
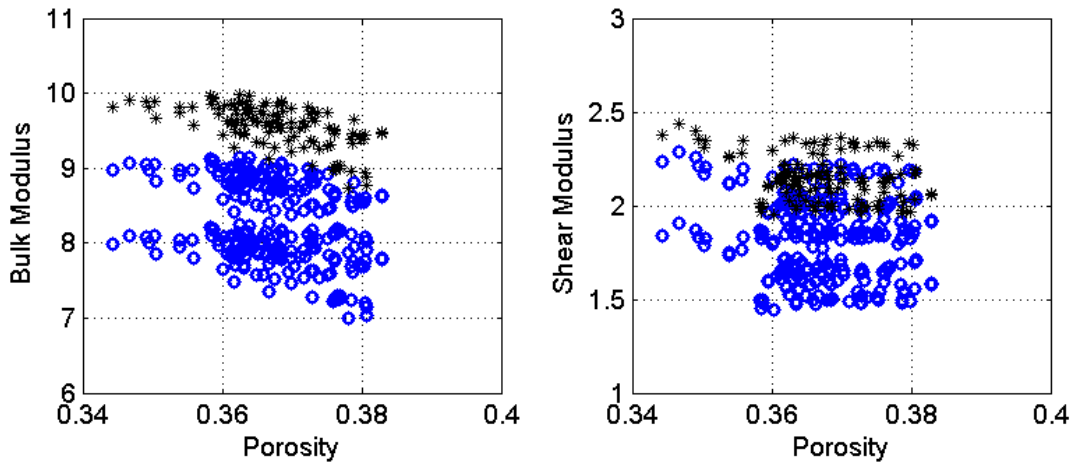
Figure 5.10: Figure 5.9 is zoomed on the area of interest: Blue points show the lower limits of the effective bulk and shear moduli saturated with water and estimated using Eqns. 5.3 and 5.4. Black color points are the actual well log data saturated with oil sand (Bulk modulus: 3.0 GPa, Shear modulus: 0.1 GPa)
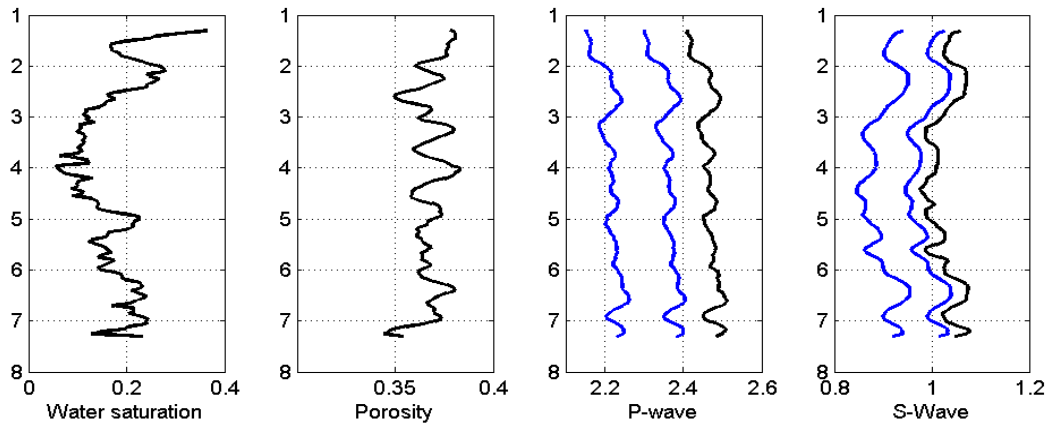
Figure 5.11: Model results vs well log data: Black curves show original well log data for an interval saturated with heavy oil. Blue curves show the lower limits of the effective bulk and shear moduli as estimated using Eqns. 5.3 and 5.4.

5.5. Chapter summary

If there is no information available on the pore space geometry of an isotropic composite with arbitrary pore geometry, our method is more effective at narrowing the range of possible solutions for effective bulk and shear moduli upon substitution than the

use of Hashin-Shtrikman bounds. Our new approach suggests a range of possible solutions with a final pore filling material. The range of soft to stiff pore filling material substitution can be interpreted as maximum when there is large strain heterogeneity in the pore space and minimum when there is strain homogeneity in the pore space. When there is a stiff to soft pore filling material substitution, then, the range of possible solutions can be explained as the maximum change corresponds to strain homogeneity in the pore space and minimum change corresponds to strain heterogeneity in the pore space.

5.6. Acknowledgements

5.7. References

Andrä, H., N. Combaret, J. Dvorkin, E. Glatt, J. Han, M. Kabel, Y. Keehm, F. Krzkilla, M. Lee, C. Madonna, M. Marsh, T. Mukerji, E. H. Saenger, R. Sain, N. Saxena, S. Ricker, A. Wiegmann and X. Zhan, 2013, Digital rock physics benchmarks - Part I: Imaging and segmentation: Computers & Geosciences, 50, 25-32.

Berge, P. A., and J. G. Berryman, 1995, Realizability of negative pore compressibility in poroelastic composites: Journal of Applied Mechanics and Technical Physics, 62, 1053–1062.

Brown, R., and J. Korringa, 1975, On the dependence of the elastic properties of a porous rock on the compressibility of the pore fluid: Geophysics, 40, 608–616.

Christensen, R. M., 1991, Mechanics of composite materials: Robert E. Krieger Publication Co.

Ciz, R., A. F. Siggins, B. Gurevich, and J. Dvorkin, 2008, Influence of microheterogeneity on effective stress properties of rocks: Geophysics, 73, no. 1, E7–E14.

Ciz, R., and S. A. Shapiro, 2007, Generalization of Gassmann equations for porous media saturated with a solid material: Geophysics, 72, A75–A79.

Gassmann, F., 1951, Über die Elastizität poröser Medien: Vierteljahrschrift der Naturforschenden Gessellschaft in Zürich, 96, 1-23.

Green, D. H., and H. F. Wang, 1986, Fluid pressure response to undrained compression in saturated sedimentary rocks: Geophysics, 51, 948–956.

Hashin, Z., 1962, The elastic moduli of heterogeneous materials, Journal of Applied Mechanics, 29, 143-150.

Hashin, Z., and S. Shtrikman, 1963, A variational approach to the elastic behavior of multiphase materials: Journal of the Mechanics and Physics of Solids, 11, 127–140.

Hart, D. J., and H. F. Wang, 2010, Variation of unjacketed pore compressibility using Gassmann's equation and an overdetermined set of volumetric poroelastic measurements: Geophysics, 75, no. 1, N9–N18.

Hill, R., 1963, Elastic properties of reinforced solids: some theoretical principles: Journal of the Mechanics and Physics of Solids, 11, 357-372.

Knackstedt, M. A., C. H. Arns, and W. Val Pinczewski, 2005, Velocity-porosity relationships: Predictive velocity model for cemented sands composed of multiple mineral phases: Geophysical Prospecting, 53, 349–372.

Makarynska, D., G. Gurevich, and R. Ciz, 2007, Finite element modeling of Gassmann fluid substitution of heterogeneous rocks: 69th Annual International Conference and Exhibition, EAGE, Extended Abstracts, 2152.

Mavko, G., T. Mukerji, and J. Dvorkin, 2009, The Rock physics handbook: Cambridge University Press.

Mavko, G., and T. Mukerji, 2013, Estimating Brown-Korringa constants for fluid substitution in multimineralic rocks: Geophysics, 78, no. 3, L27-L35.

Chapter 6

Analysis of Rock Physics Inclusion Models

6.1. Abstract

In this chapter, we study four different effective medium theory (EMT) models: Self-Consistent (SC), Differential Effective Medium (DEM), Mori-Tanaka (MT), and Kuster-Toksoz (KT). We plot a wide range of different aspect ratios (AR) for each model between Hashin-Shtrikman bounds (HS) to analyze certain gaps. We also perform fluid and solid substitution to observe how each model performs. In addition, we show what model captures more heterogeneity in the pore space, which we assume to be inclusions in EMT models.

6.2.   Introduction

Inclusion models approximate rock as a continuous elastic solid containing solid or fluid inclusions. The solid inclusions may represent solid grains, and the fluid inclusions represent the rock pore space. Mineral inclusions stiffer than the rock matrix stiffen the rock, while softer inclusions, such as fluid and soft minerals, soften the rock. Most of the inclusion models treat the pores as ellipsoids (Eshelby, 1957; Walsh, 1965; Eimer, 1967, 1968; Kuster and Toksoz, 1974; O'Connell and Budiansky, 1974, 1977; Cheng, 1978, 1993; Berryman, 1980; Norris, 1985a; Hudson, 1980, 1981, 1990; Hudson and Liu, 1999; Crampin, 1984; Johansen et al., 2002; Jakobsen et al. 2003). Berryman (1980) generalized the self-consistent formulation so that both the pores and the grains are considered ellipsoidal inclusions in the composite material.

The differential effective medium (DEM) theory models two-phase composites by incrementally adding inclusions of one phase to the matrix phase (Cleary et al., 1980; Norris, 1985; Zimmerman, 1991). Schoenberg (1983) and Pyrak-Nolte et al. (1990a, b) have considered inclusions in the form of infinite planes of slip or compliance, to model fractures.

The key assumption in the Mori-Tanaka (MT) model (1973) is that the average strain in the inclusion is related to the average strain in the matrix by a fourth order tensor. This fourth order tensor gives the relation between the uniform strain in the inclusion embedded in an all matrix material. Further, this material is subjected to uniform strain at infinity.

The Kuster-Toksöz theory (Kuster and Toksöz, 1974) is based on the long wavelength, first-order scattering phenomena of elastic waves in a two-phase medium. The medium is assumed to consist of solid matrix and inclusions. KT assumes that the pores are isolated and do not interact, and hence this model is limited to a dilute concentration of pores, which means the porosity cannot be too high.

Some studies have shown that the SC model always falls between HS bounds. The two-phase DEM model might not always fall between HS bounds for some inclusion types. MT can violate HS bounds when there are three or more phases. KT can also violate HS bounds when inclusions are either disks at any finite concentration or needles at volume fraction greater than 60%.

In this paper, we focus on four EMT models composed of two phases: solid matrix and inclusions (pores). We explore the limits of each model by looking at the areas that are not covered within HS bounds. We also perform fluid and solid substitution for each model. We, then, compare results to understand the change in effective bulk and shear moduli. Using recently derived *exact* solid substitution equations by Saxena and Mavko (2013) we can analyze which model captures more heterogeneity in the pore space. These exact equations make use of *pore compliance parameters*, which are presented in a computationally convenient form. For fluid-to-solid substitution of the bulk modulus,

$$\left(K_{p_1} - K_{p_2}\right)\alpha_1 + \left(G_{p_1} - G_{p_2}\right)\alpha'_2 = \phi\frac{\left(K_m - K_{p_2}\right)\left(K_m - K_{p_1}\right)}{\left(K_m - K_{sat1}\right)\left(K_m - K_{sat2}\right)}\left(K_{sat1} - K_{sat2}\right) \qquad , \qquad (6.1)$$

where

$$\alpha_1 = \frac{\overline{P^{p_1}P^{p_2}}}{P^{p_1}P^{p_2}} \quad \alpha_2 = \frac{1}{2}\frac{\overline{\tau_{ij}^{p_1}\tau_{ij}^{p_2}}}{P^{p_1}P^{p_2}} \qquad ,$$

and

$$\alpha_2' = \frac{K_{p_1}K_{p_2}}{G_{p_1}G_{p_2}}\alpha_2 \qquad ,$$

where α_2' depends on α_2.

For effective shear modulus

$$\left(G_{p_1} - G_{p_2}\right)\beta_1 + \left(K_{p_1} - K_{p_2}\right)\beta_2' = \phi\frac{\left(G_m - G_{p_2}\right)\left(G_m - G_{p_1}\right)}{\left(G_m - G_{sat2}\right)\left(G_m - G_{sat1}\right)}\left(G_{sat1} - G_{sat1}\right) \qquad , \qquad (6.2)$$

where

$$\beta_1 = \frac{1}{2}\frac{\overline{\tau_{ij}^{p_1}\tau_{ij}^{p_2}}}{\tau_{12}^{p_1}\tau_{12}^{p_2}} \qquad \beta_2 = \frac{\overline{P^{p_1}P^{p_2}}}{\tau_{12}^{p_1}\tau_{12}^{p_2}} \qquad ,$$

and

$$\beta_2' = \frac{G_{p_1}G_{p_2}}{K_{p_1}K_{p_2}}\beta_2 \qquad .$$

In Eqns. 6.1 and 6.2, ϕ is the porosity, K_{p_1} and G_{p_1} are the bulk and shear moduli of

the initial pore-filling solid, K_{p_2} and G_{p_2} are the bulk and shear moduli of the final

pore-filling solid, K_m and G_m are the bulk and shear moduli of the mineral in the rock

frame, K_{sat1} and G_{sat1} are the effective bulk and shear moduli of the initial-filled composite, and K_{sat2} and G_{sat2} are the effective bulk and shear moduli of the final-filled composite. $P^{p_{1,2}}$ is the volumetric induced stress in the initial and final pore filling materials, respectively, and $\tau_{ij}^{p_{1,2}}$ is the shear-induced stress in the initial and final pore filling materials, respectively ($\overline{\Psi}$ denotes the pore volume average of parameter Ψ). It is guaranteed that α_1, β_1 ≥ 1 and α_2, $\beta_2 \geq 0$. Furthermore, when α_1, β_1 = 1 and α_2, β_2 = 0 equations suggest that induced stress in the pore space is homogenous. Hence, we invert results from each solid substitution into estimating α_1, β_1 and α_2, β_2.

6.3. Analysis of inclusion models

6.3.1. Pore space saturated with fluid

As we mentioned before in this study we compose EMT model with *two phases*: a solid phase – matrix and a pore phase – inclusions. In this paper, we set solid phase as quartz with bulk modulus of 37 GPa and shear modulus of 44 GPa. We, then, vary aspect ratio (AR) of inclusions from oblate to prolate spheroids with the range of 0.001–2 and step of 0.001. The pore filling material is a fluid with bulk modulus of 2.2 GPa and shear modulus of 0 GPa. We plot SC, DEM, MT and KT along with Hashin-Shtrikman bounds.

Figure 6.1 shows result of SC model plotted between HS bounds. There is one significant gap (highlighted in transparent blue color) between the largest AR and upper

HS bound for both bulk and shear moduli. Note that here we only consider varying AR of

inclusions in SC model. However, previous studies have shown that varying AR of both

inclusions and grains will fill up those gaps. That is only applicable in SC model.

Figure 6.1: *Fluid saturated case.* Blue color lines are Self-Consistent effective bulk modulus on the left and effective shear modulus on the right with AR varying from 0.001-2. The black solid and dashed lines are HS upper and lower bound, respectively. Transparent blue color highlights the gaps between SC model and HS bounds.

Figure 6.2 shows that in the case of DEM model the gap between the largest AR and

upper HS bound seems to be less wide than in SC model.

Figure 6.2: *Fluid saturated case.* Blue color lines are DEM effective bulk modulus on the left and effective shear modulus on the right with AR varying from 0.001-2. The black solid and dashed lines are HS upper and lower bound, respectively. Transparent blue color highlights the gaps between DEM model and HS bounds.

The Mori-Tanaka model covers most of the area between HS bounds for both effective bulk and shear moduli. There is, however, insignificant gap that appears in effective shear modulus between lowest AR and lower HS bound (Figure 6.3). In order to model that small gap, we would have to lower the step for AR to 0.0001, which, also, implies that MT model is quite sensitive with a small change in AR.
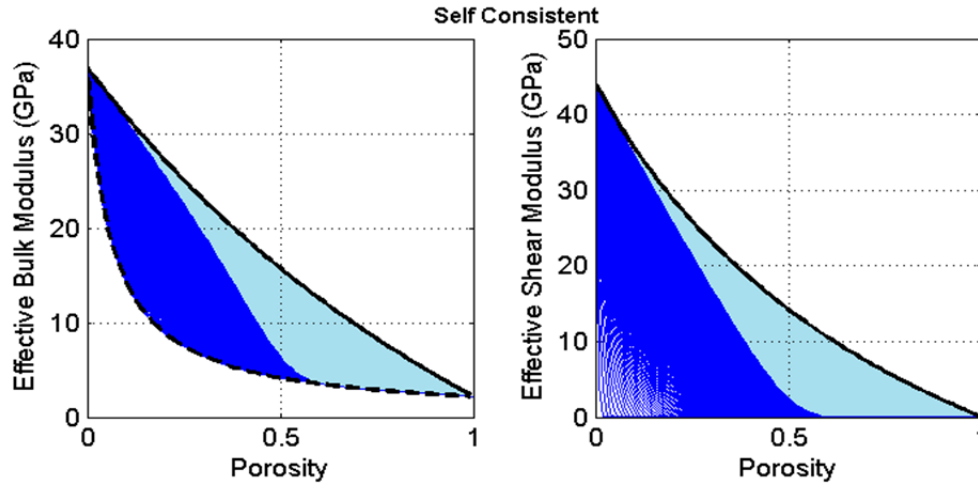
Figure 6.3: *Fluid saturated case.* Blue color lines are Mori-Tanaka effective bulk modulus on the left and effective shear modulus on the right with AR varying from 0.001-2. The black solid and dashed lines are HS upper and lower bound, respectively.

On Figure 6.4 we show results from Kuster-Toksoz model for both effective bulk and shear moduli. It shows that for pores/inclusions filled with fluid some KT lines fall outside of HS lower bound for effective bulk modulus.
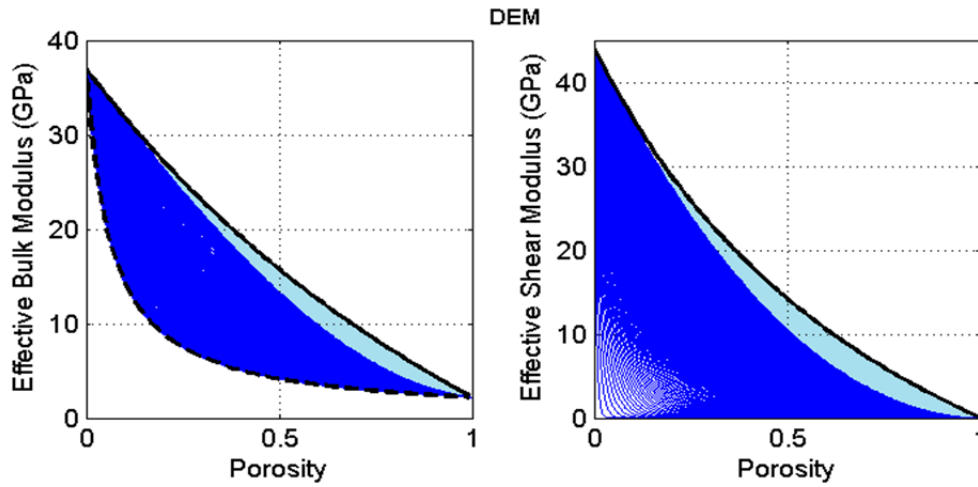

Figure 6.4: *Fluid saturated case.* Blue color lines are Kuster-Toksoz effective bulk modulus on the left and effective shear modulus on the right with AR varying from 0.001-2. The black solid and dashed lines are HS upper and lower bound, respectively.

6.3.2. Pore space saturated with solid

We repeat the same experiment but with solid pore/inclusions filling material. We, again, compose EMT model with *two phases*: a solid phase – matrix and a pore phase – inclusions. We set the matrix phase as quartz with bulk modulus of 37 GPa and shear modulus of 44 GPa. We, then, vary aspect ratio of pores/inclusions from oblate to prolate spheroids with the range of 0.001–2 and step of 0.001 and set pore space as a solid with bulk modulus of 3.2 GPa and shear modulus of 1 GPa. We plot SC, DEM, MT and KT along with Hashin-Shtrikman bounds.

We, now, observe two significant gaps on Figure 6.5 for SC model (highlighted in transparent blue color) between the smallest AR and lower HS bound, the largest AR and upper HS bound for both bulk and shear moduli.
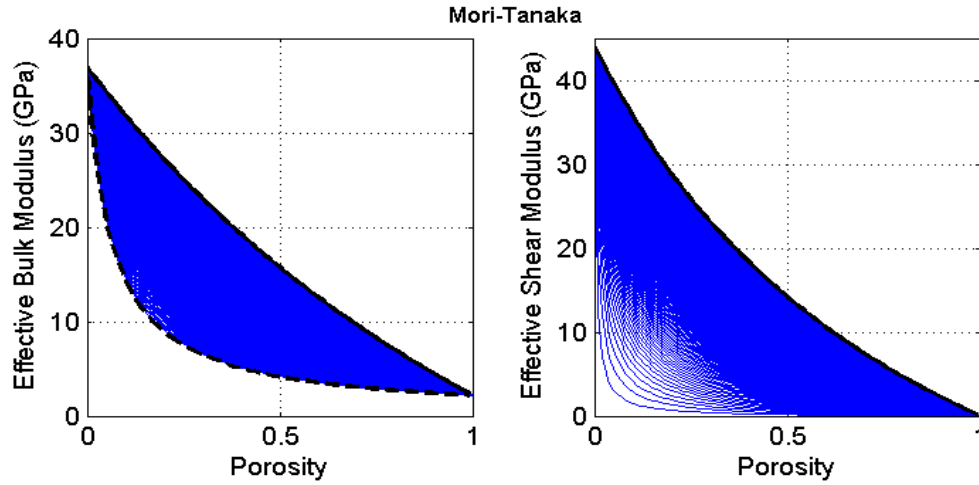

Figure 6.5: *Solid saturated case.* Blue color lines are Self-Consistent effective bulk modulus on the left and effective shear modulus on the right with AR varying from 0.001-2. The black solid and dashed lines are HS upper and lower bound, respectively. Transparent blue color highlights the gaps between SC model and HS bounds.

The DEM model, on Figure 6.6 again, has the gap between the largest AR and upper

HS bound seems to be less wide than in SC model. The gap also seems to be similar to
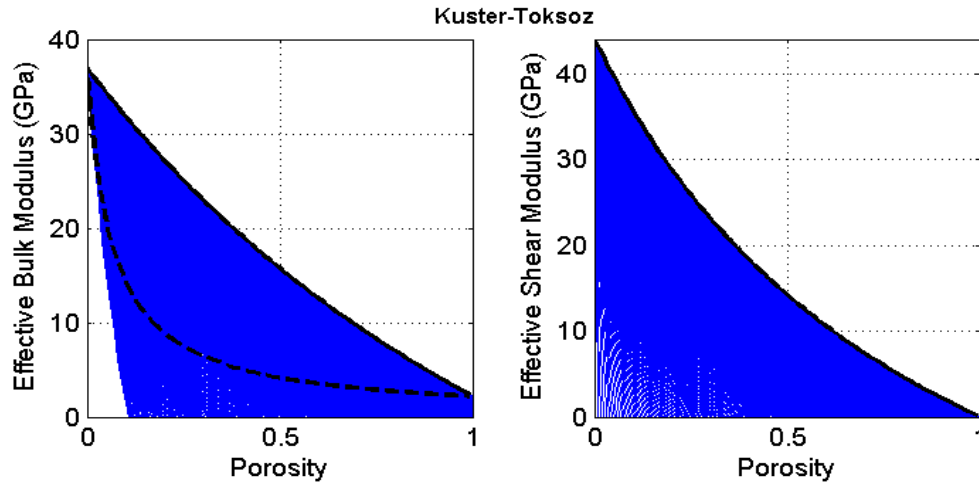
pore/inclusions saturated with fluid.

Figure 6.6: *Solid saturated case.* Blue color lines are DEM effective bulk modulus
on the left and effective shear modulus on the right with AR varying from
0.001-2. The black solid and dashed lines are HS upper and lower bound,
respectively. Transparent blue color highlights the gaps between DEM model
and HS bounds.

Mori-Tanaka model for inclusions/pores filled with solid covers the entire of the area

between HS bounds for both effective bulk and shear moduli (Figure 6.7).

Figure 6.7: *Solid saturated case.* Blue color lines are Mori-Tanaka effective bulk modulus on the left and effective shear modulus on the right with AR varying from 0.001-2. The black solid and dashed lines are HS upper and lower bound, respectively.

Results from Kuster-Toksoz model for both effective bulk and shear moduli show that all the area between HS bounds is covered, however, a major part of the model falls outside of HS lower bound for effective bulk and shear modulus.
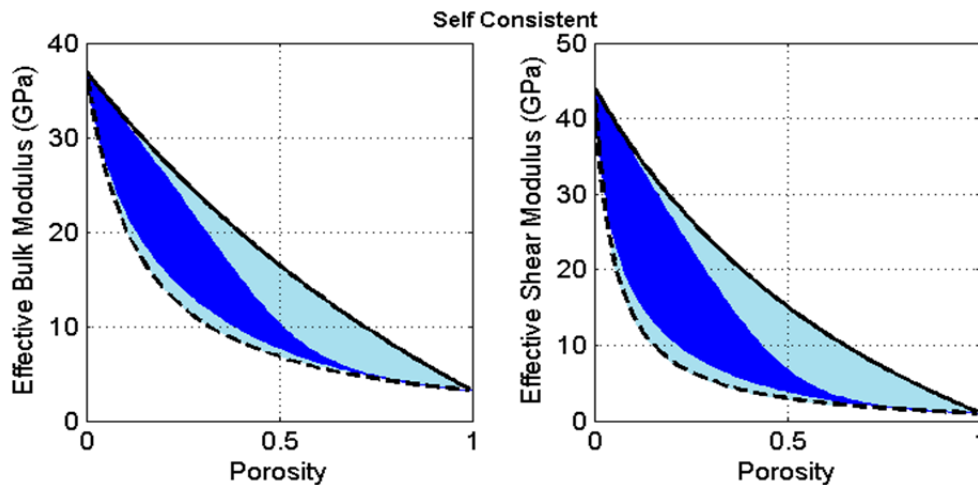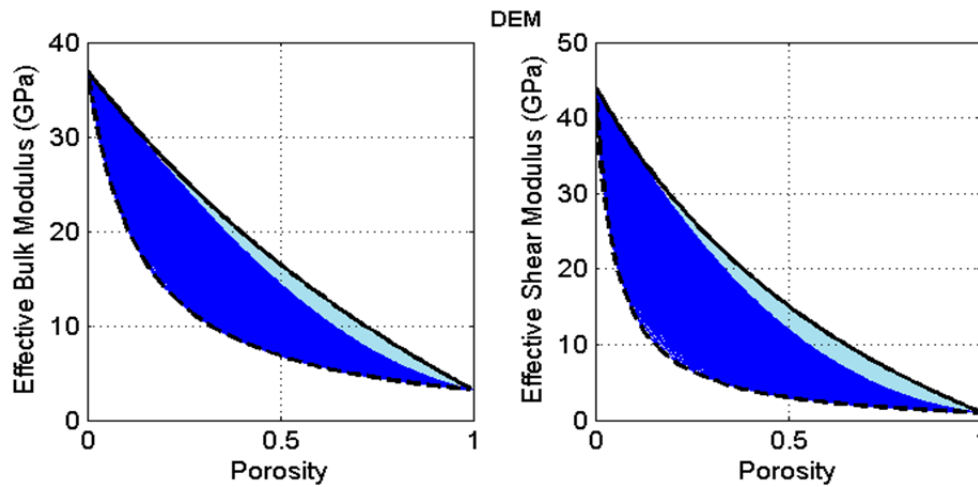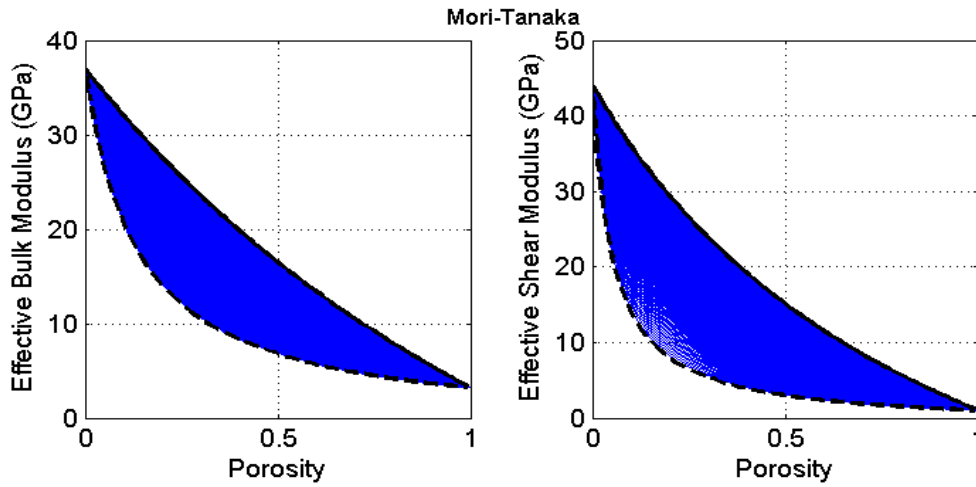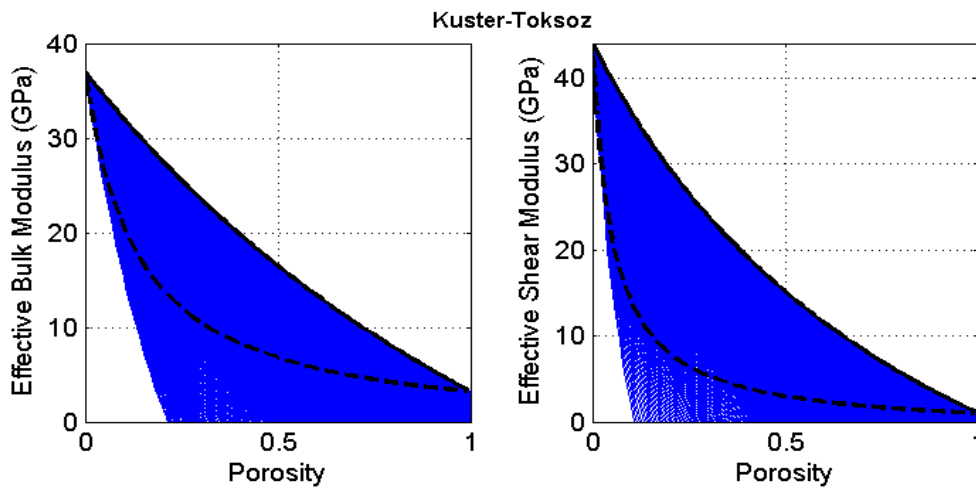

Figure 6.8: *Solid saturated case.* Blue color lines are Kuster-Toksoz effective bulk modulus on the left and effective shear modulus on the right with AR varying from 0.001-2. The black solid and dashed lines are HS upper and lower bound, respectively.

6.4. Solid and fluid substitution with inclusion models

We, now, study how each effective theory models fits with Gassmann (1951) and Ciz and Shapiro (2007) (C&S) models. From Han's laboratory measurements of dry Berea sandstone, we select one of the points for effective bulk (14.44 GPa) and shear moduli (12.65 GPa) with porosity of 0.2215 and it is denoted on Figure 6.9 as a black circle. We, then, fit dry Berea sandstone point at porosity 0.2215 with each EMT model of SC (dashed red line), DEM (dashed blue line), MT (dashed black line) and KT (dashed green line). Corresponding ARs for each model are listed in Table 6.1 for effective bulk and shear moduli. We observe that for effective bulk modulus and effective shear modulus we have to fit EMT models with slightly different ARs.

Table 6.1: A list of ARs for each EMT models for effective bulk and shear modulus
of dry Berea sandstone point with porosity 0.2215 with.

EMT models:	AR for Effective Bulk modulus	AR for Effective Shear modulus
SC	0.18536	0.15133
DEM	0.14885	0.10671
MT	0.09535	0.05335
KT	0.15403	0.10270

Next, using Gassmann's equation we substitute dry Berea sandstone point, assuming that the mineral matrix is pure quartz (bulk: 37 GPa, shear: 44 GPa) and the pore filling material is air (bulk: 0 GPa, shear: 0 GPa), with fluid pore filling material (bulk: 2.2 GPa, shear: 0 GPa). Result of substituted dry-to-fluid pore filling material point is shown on Figure 6.9 as a black asterisk. Using exactly the same ARs listed in Table 6.1 and the same mineral matrix as pure quartz, we only change the pore/inclusion filling material to fluid material (bulk: 2.2 GPa, shear: 0 GPa) in each EMT models. On Figure 6.9 we

display each EMT with fluid saturated pore space as following: SC is a solid red line, DEM is a solid blue line, MT is a solid black line, and KT is a solid green line.

On Figure 6.10 we see a closer look of the result of our experiment. We observe that Gassmann effective bulk modulus saturated with fluid (black asterisk) falls exactly on EMT models such as MT (solid black line) and KT (solid green line), however, SC (solid red line) and DEM (solid blue line) overestimate the change in dry-to-fluid substitution by ~ 0.5 GPa. Furthermore, all four of the EMT models fail to predict *no* change in dry-to-fluid substitution for effective shear modulus. The approximate overestimation is 1 GPa for MT and KT models, 2 GPa for DEM model and 3 GPa for SC model.
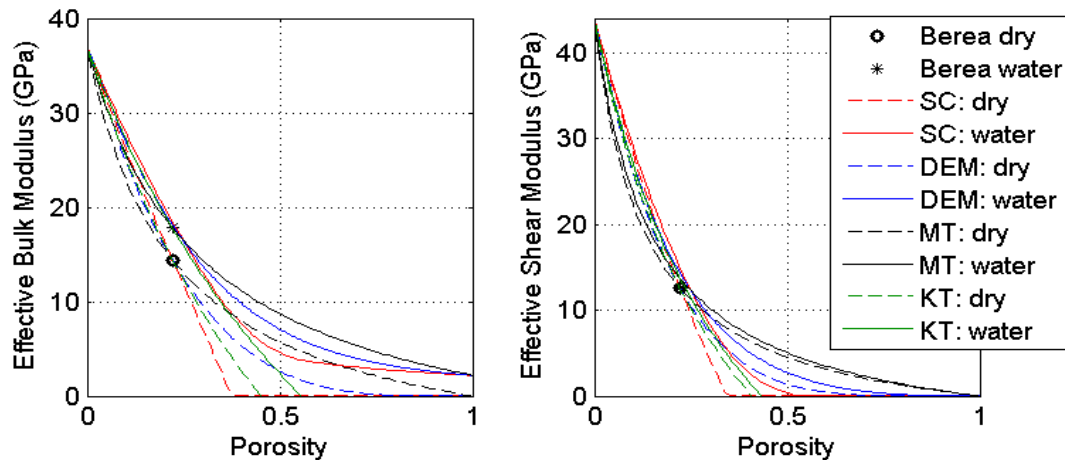
Figure 6.9: *Dry-to-Fluid substitution.* The black circle is original dry Berea sandstone point from Han's lab measurements. The black asterisk is a result of Gassmann's fluid substitution. The red color lines are SC model. The blue color lines are DEM model. The black color lines are MT model and the green color lines are KT model. The dashed lines represent the fitted EMT models for the original dry Berea sandstone point. The solid lines are the same EMT models but saturated with fluid.

Figure 6.10: *Dry-to-Fluid substitution.* Zoomed on the area of interested on Figure 6.9.

Gassmann water saturated Berea sandstone point (shown on Figure 6.11 as a black circle) is, now, matched with each EMT model of SC (dashed red line), DEM (dashed blue line), MT (dashed black line) and KT (dashed green line) at porosity 0.2215. Corresponding ARs for each model are listed in Table 6.2:

Table 6.2: A list of ARs for each EMT models for effective bulk and shear modulus saturated with water of Berea sandstone point with porosity 0.2215

EMT models:	AR for Effective Bulk modulus	AR for Effective Shear modulus
SC	0.167606	0.117185
DEM	0.142456	0.088915
MT	0.095283	0.04540
KT	0.153968	0.093982

Now, using C&S equation we substitute fluid saturated Berea sandstone point, assuming the same mineral matrix as pure quartz (bulk: 37 GPa, shear: 44 GPa) and the pore filling material is water (bulk: 2.2 GPa, shear: 0 GPa), with heavy oil pore filling material (bulk: 2.5 GPa, shear: 0.4 GPa). The result of substituted fluid-to-solid pore filling material point is shown on Figure 6.10 as a black asterisk and referred as heavy oil (ho). For each EMT model, using exactly the same ARs listed in Table 6.2 and the same

mineral matrix as pure quartz, we only change the pore/inclusion filling material to heavy oil. On Figure 6.11 we display each EMT with heavy oil saturated pore space as following: SC is a solid red line, DEM is a solid blue line, MT is a solid black line, and KT is a solid green line.

On Figure 6.12 we see a closer look of the result of our experiment. We observe that the C&S effective bulk and shear moduli saturated with solid (black asterisk) does not fall on any EMT models. The approximate underestimation of C&S solid substitution for effective bulk modulus is 1 GPa for MT and KT models, 1.5 GPa for DEM model and 2 GPa for SC model; effective shear modulus is 2 GPa for MT and KT models, 3 GPa for DEM model and 4 GPa for SC model.
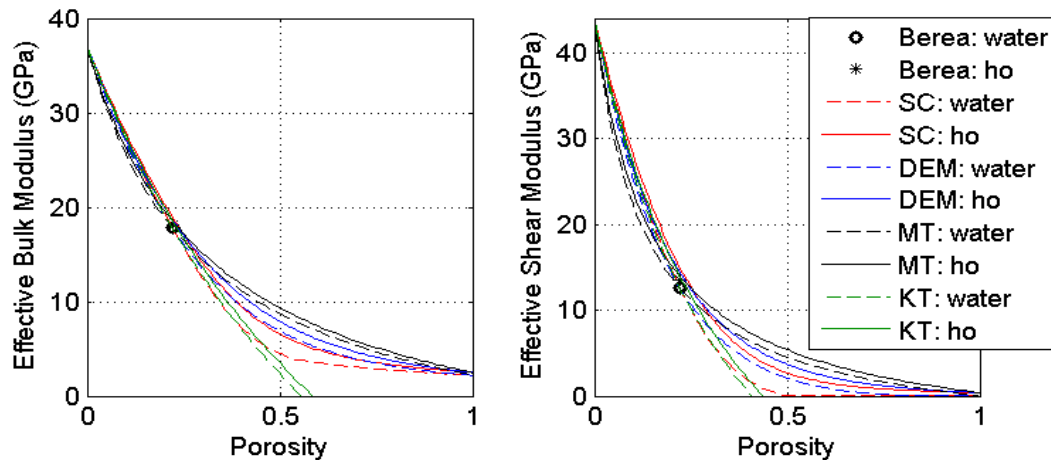
Figure 6.11: *Water-to-Heavy Oil substitution.* The black circle is water Berea sandstone point from Gassmann substitution. The black asterisk is a result of C&S solid substitution. The red color lines are SC model. The blue color lines are DEM model. The black color lines are MT model and the green color lines are KT model. The dashed lines represent the fitted EMT models for the water Berea sandstone point. The solid lines are the same EMT models but saturated with heavy oil (ho).
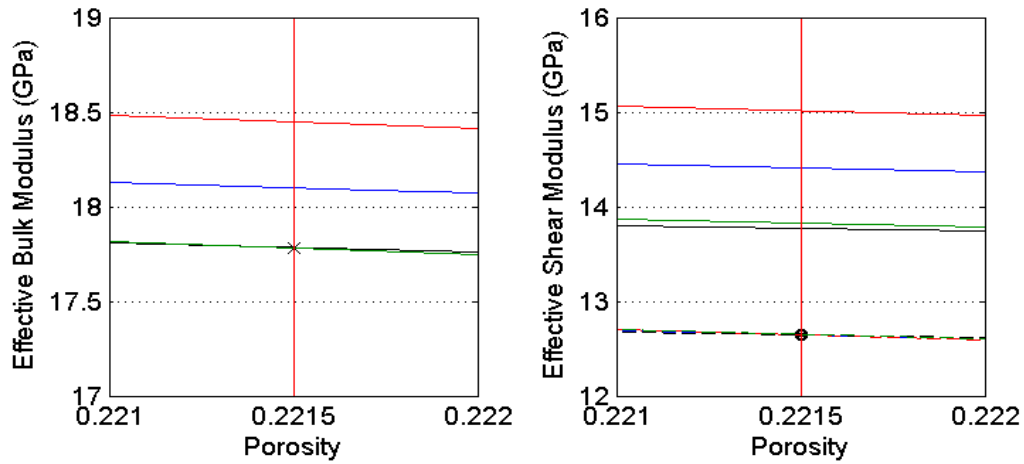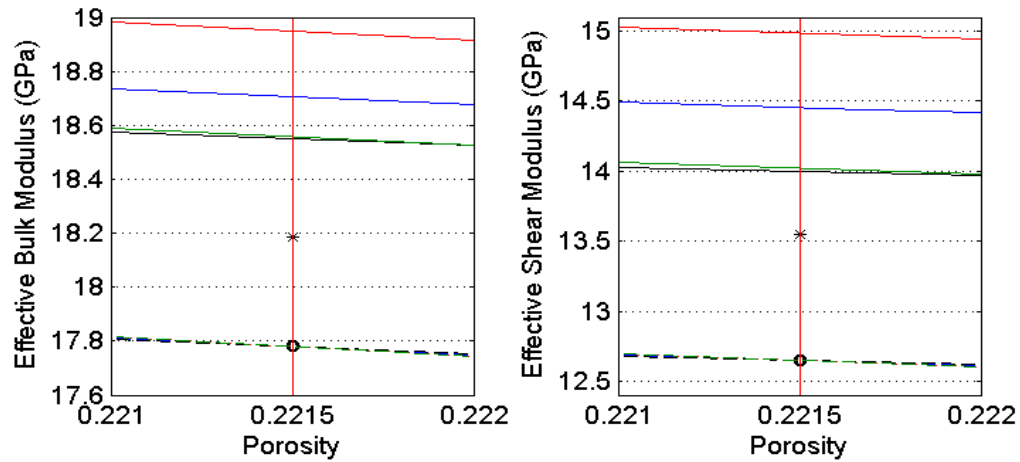
Figure 6.12: *Water-to-Heavy Oil substitution.* Zoomed on the area of interested on Figure 6.11.

To understand approximately where fluid-to-solid substitution of Berea sandstone point with porosity of 0.2215 should fall on the plot we refer to Aliyeva and Gary 2015 paper. In the paper, we borrow a figure (Figure 6.13) of numerical simulated effective bulk and shear moduli of 5 sub-samples saturated with water (blue color lines) (bulk: 2.2 GPa, shear: 0 GPa) and heavy oil (black color lines) (bulk: 2.5 GPa, shear: 0.4 GPa), assuming that the mineral matrix is pure quartz (bulk: 37 GPa, shear: 44 GPa). We also perform C&S fluid-to-solid substitution shown in red color lines.

From Figure 6.13 we observe that C&S approximation falls half way between initial pore filling material (water saturated Berea sandstone 5 points) and final pore filling material (heavy oil saturated Berea sandstone 5 points). Assuming that this is true for all Berea sandstone points we can conclude from Figure 6.12 that C&S approximation (black asterisk) is a half way between initial and final pore filling material. This suggests that effective bulk and shear modulus of Berea sandstone point of porosity 0.2215

saturated with heavy oil (bulk: 2.5 GPa, shear: 0.4 GPa) falls approximately at DEM model saturated with heavy oil.

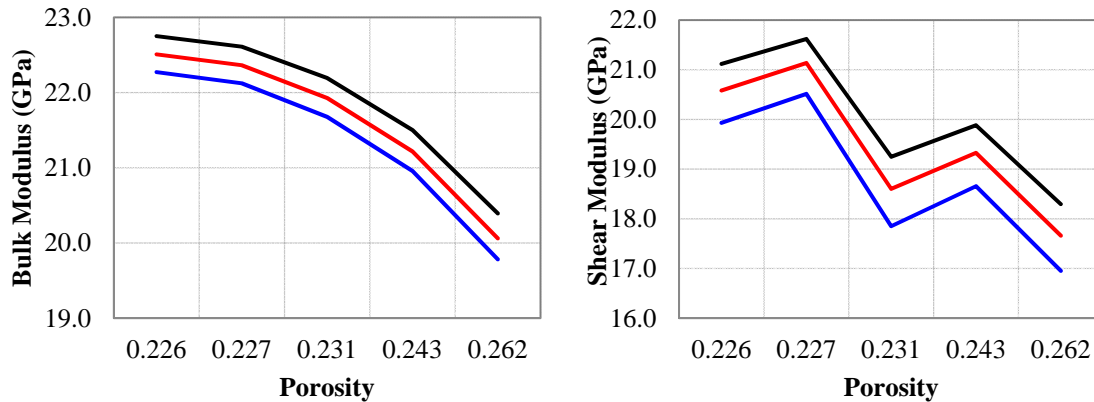Figure 6.13: Berea sandstone: Effective bulk modulus on the left, effective shear modulus on the right. Blue color curves are numerically estimated effective elastic properties of sandstone sub-samples saturated with water. Black color curves are numerically estimated effective elastic properties of sandstone sub-samples saturated with heavy oil. Red color curves are substituted water with heavy oil pore filling material using the Ciz and Shapiro approximation.

To understand if there might be a larger change between four EMT models from initial pore filling material we increase bulk and shear moduli for the final pore filling material. Next, using the C&S approximation we substitute dry Berea sandstone point, assuming that the mineral matrix is pure quartz (bulk: 37 GPa, shear: 44 GPa) and the pore filling material is air (bulk: 0 GPa, shear: 0 GPa), with solid pore filling material (bulk: 5 GPa, shear: 3 GPa). Result of substituted dry-to-fluid pore filling material point is shown on Figure 6.14 as a black asterisk. Using exactly the same ARs listed in Table 6.1 and the same mineral matrix as pure quartz, we only change the pore/inclusion filling material to solid material in each EMT models. On Figure 6.14 we display each EMT with solid (kerogen) saturated pore space as following: SC is a solid red line, DEM is a solid blue line, MT is a solid black line, and KT is a solid green line.

On Figure 6.15 we see a closer look of the result of our experiment. We observe that the C&S effective bulk and shear moduli saturated with solid (black asterisk) do not fall on any EMT models. The approximate underestimation of C&S solid substitution for effective bulk modulus is 1 GPa for MT and KT models, 1.5 GPa for DEM model and 2 GPa for SC model; effective shear modulus is 3 GPa for MT and KT models, 4 GPa for DEM model and 5 GPa for SC model.
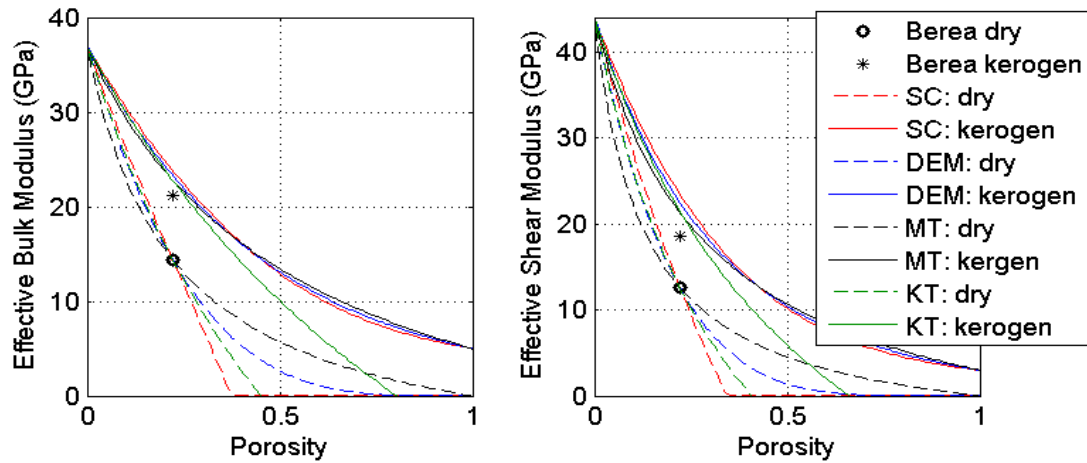
Figure 6.14: *Dry-to-Kerogen substitution.* The black circle is dry Berea sandstone point from Han's lab measurements. The black asterisk is a result of C&S solid substitution. The red color lines are SC model. The blue color lines are DEM model. The black color lines are MT model and the green color lines are KT model. The dashed lines represent the fitted EMT models for the dry Berea sandstone point. The solid lines are the same EMT models but saturated with kerogen.
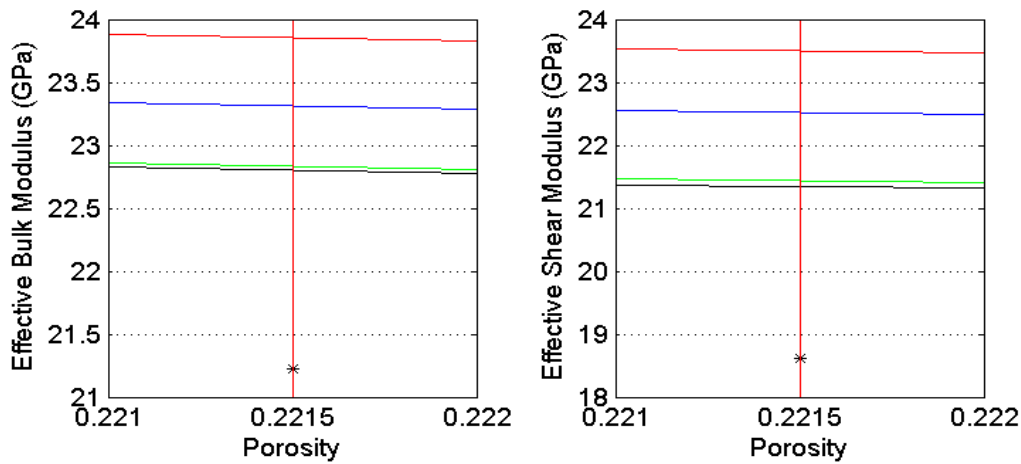
Figure 6.15: *Dry-to-Kerogen substitution.* Zoomed on the area of interested on Figure 6.14.

Interestingly, no matter what material we use to replace initial with a final pore filling material keeping the same ARs, there always seems to be a pattern between each model. It appears that the smallest change from substitution point is always MT and KT whereas DEM and SC have the largest change.

6.5.   Homogeneity in the pore space

It is interesting to see how much heterogeneity in the pore space each model captures. Hence, we refer to Saxena and Mavko *pore compliance parameters.* In their paper, they state that if α_1, $\beta_1 = 1$ and α_2, $\beta_2 = 0$ in the Eqns 6.1 and 6.2 it suggests that induced stress in the pore space is homogenous and hence Eqns 6.1 and 6.2 become Ciz and Shapiro.   We, now, calculate pore compliance parameters. However, there are two unknowns in the Eqn 6.1 α_1 and α_2, in the Eqn 6.2 it is β_1 and β_2. To overcome this issue, we fix shear modulus with initial (bulk: 0 GPa, shear: 0 GPa) and final (bulk: 3.2

GPa, shear: 0 GPa) pore filling material, then we get following modified Eqns 6.1 and 6.2

as:

$$\left(K_{p_1}-K_{p_2}\right)\alpha_1 = \phi\frac{\left(K_m-K_{p_2}\right)\left(K_m-K_{p_1}\right)}{\left(K_m-K_{sat1}\right)\left(K_m-K_{sat2}\right)}\left(K_{sat1}-K_{sat2}\right) \qquad , \qquad (6.3)$$

$$\left(K_{p_1}-K_{p_2}\right)\beta_2' = \phi\frac{\left(G_m-G_{p_2}\right)\left(G_m-G_{p_1}\right)}{\left(G_m-G_{sat2}\right)\left(G_m-G_{sat1}\right)}\left(G_{sat1}-G_{sat1}\right) \qquad , \qquad (6.4)$$

Next, to estimate α_2, β_1. we fix bulk modulus with initial (bulk: 3.2 GPa, shear: 0 GPa) and final (bulk: 3.2 GPa, shear: 1 GPa) pore filling material, then we get following modified Eqns 6.1 and 6.2 as:

$$\left(G_{p_1}-G_{p_2}\right)\alpha_2' = \phi\frac{\left(K_m-K_{p_2}\right)\left(K_m-K_{p_1}\right)}{\left(K_m-K_{sat1}\right)\left(K_m-K_{sat2}\right)}\left(K_{sat1}-K_{sat2}\right) \qquad , \qquad (6.5)$$

$$\left(G_{p_1}-G_{p_2}\right)\beta_1 = \phi\frac{\left(G_m-G_{p_2}\right)\left(G_m-G_{p_1}\right)}{\left(G_m-G_{sat2}\right)\left(G_m-G_{sat1}\right)}\left(G_{sat1}-G_{sat1}\right) \qquad , \qquad (6.6)$$

Hence, we get just one unknown in each equation. Using each effective bulk and shear moduli from SC, DEM, MT and KT with initial and finial pore filling material we now can estimate α_1, β_2 and then α_2', β_1.

We, first, focus on estimating α_1 and β_2 using Eqns. 6.3 and 6.4. We fix AR for each EMT models as 1. The results of effective bulk and shear modulus with initial (bulk: 0 GPa, shear: 0 GPa) and finial (bulk: 3.2 GPa, shear: 0 GPa) pore filling material for each model with AR 1 are shown on Figure 6.16. We focus on specific porosity of 0.2215 and draw a black vertical line on Figure 6.16. We also assume that the solid matrix is pure quartz (bulk: 37 GPa, shear: 44 GPa).

On Figure 6.17 we observe that the smallest change (~ 1GPa) in effective bulk modulus corresponds to MT and KT, which fall on top of each other. The largest change corresponds to SC, which is approximately 2 GPa. There is also a small change in effective shear modulus for SC and DEM. However, models such as MT and KT show no change in effective shear modulus. Hence, we should expect to see some heterogeneity in α_1 and β_2 in SC and DEM presented $\alpha_1 > 1$ and $\beta_2 > 0$

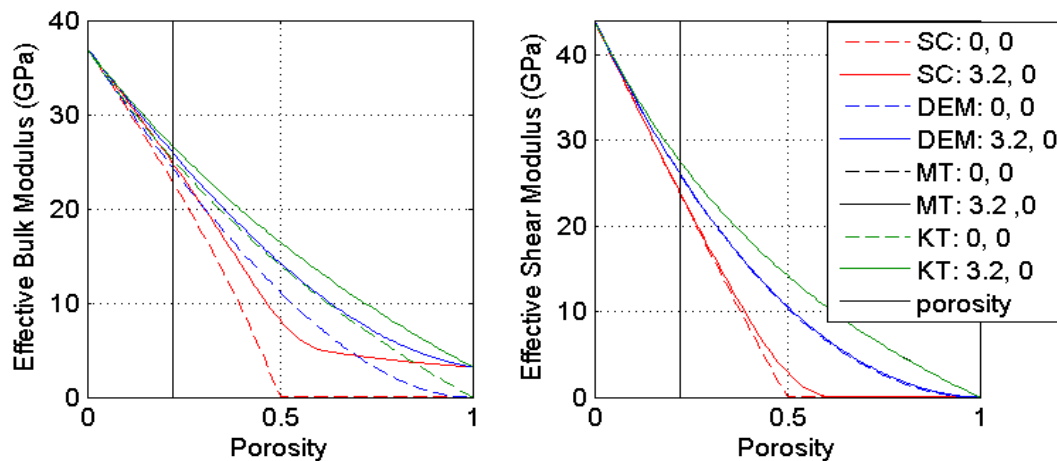Figure 6.16: *Effective bulk and shear modulus for estimation of* α_1, β_2. The black vertical line is a point of interest with porosity 0.2215. The red color lines are SC model. The blue color lines are DEM model. The black color lines are MT model and the green color lines are KT model. The dashed lines represent initial pore filling material and the solid lines are the final pore filling material.

Figure 6.17: *Effective bulk and shear modulus for estimation of* α_1, β_2. Zoomed on
the area of interested on Figure 6.16.

Next, we estimate α_2' and β_1 using Eqns. 6.5 and 6.6. We fix AR for each EMT

models as 1. The results of effective bulk and shear modulus with initial (bulk: 3.2 GPa,

shear: 0 GPa) and finial (bulk: 3.2 GPa, shear: 1 GPa) pore filling material for each

model with AR 1 are shown on Figure 6.18. We focus on specific porosity of 0.2215 and

draw a black vertical line on Figure 6.16. We also assume that the solid matrix is pure

quartz (bulk: 37 GPa, shear: 44 GPa).

On Figure 6.19 we observe that the smallest change (~ 0.5 GPa) in effective shear

modulus corresponds to MT and KT, which again fall on top of each other. The largest

change corresponds to SC, which is approximately 1 GPa. There is also a small change

in effective bulk modulus for SC and DEM. MT and KT show no change in effective

bulk modulus. Hence, we should expect to see some heterogeneity in α_2' and β_1 in SC

and DEM presented $\alpha_2' > 0$ and $\beta_1 > 1$.

Figure 6.18: *Effective bulk and shear modulus for estimation of α'_2, β_1. The black vertical line is a point of interest with porosity 0.2215. The red color lines are SC model. The blue color lines are DEM model. The black color lines are MT model and the green color lines are KT model. The dashed lines represent initial pore filling material and the solid lines are the final pore filling material.*
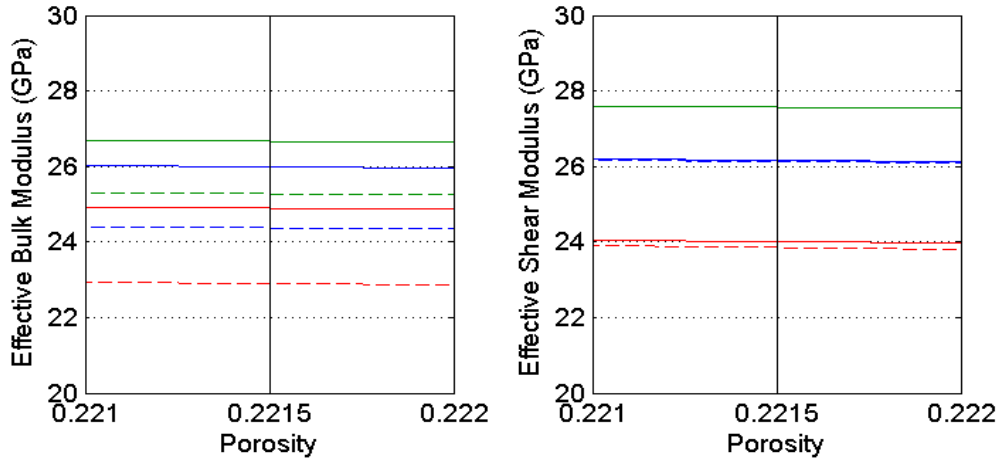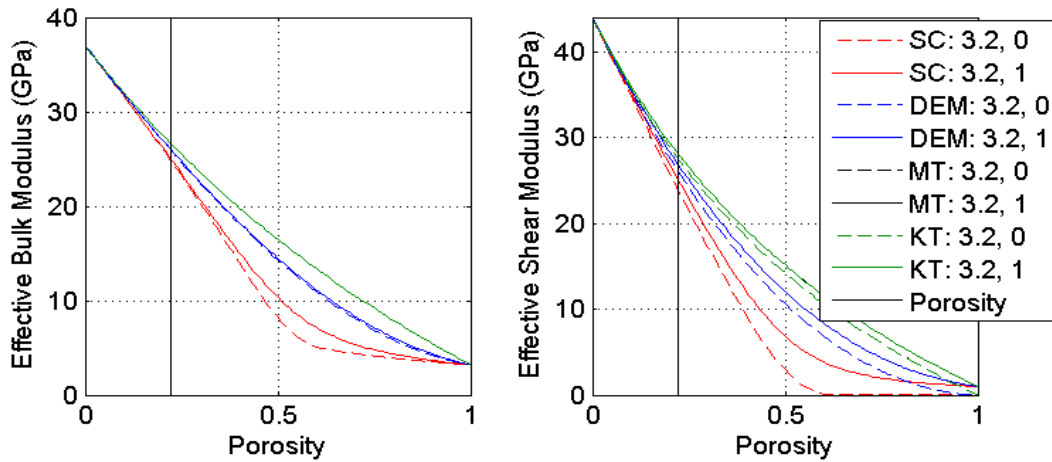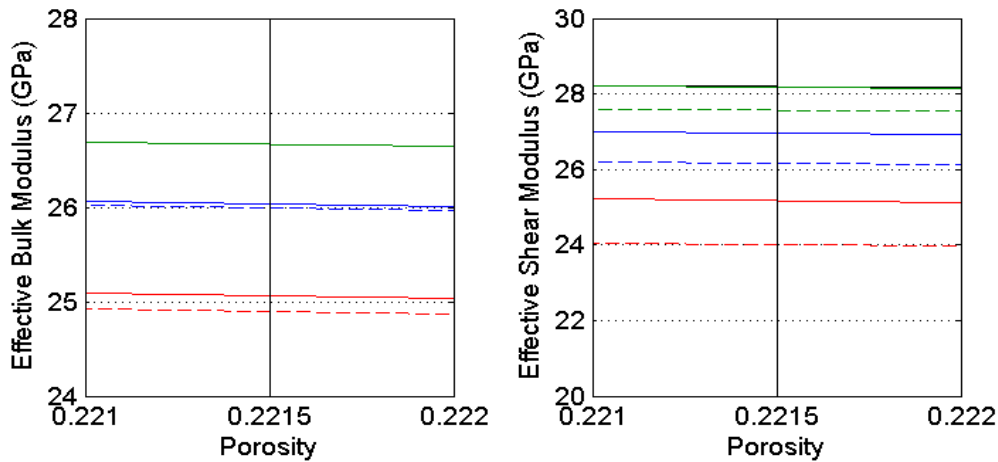

Figure 6.19: *Effective bulk and shear modulus for estimation of α'_2, β_1. Zoomed on the area of interested on Figure 6.18.*

Results for each model and estimated α_1, β_2 and then α'_2, β_1 are shown on Table 6.3. Here, we observe exactly what we expected to see. For models such as SC and DEM $\alpha_1, \beta_1 > 1$ and $\alpha'_2, \beta_2 > 0$ which implies that even though induced stress has to be homogenous in pore space with AR=1, it does not apply for SC and DEM. Whereas MT and KT present perfect homogeneity in the pore space with AR=1.

Table 6.3: Pore compliance parameters for each EMT models

EMT	α_1	α_2'	β_1	β_2'
Mori-Tanaka	1.0	0	1	0
Kuster-Toksoz	1.0	0	1	0
DEM	1.0	0.1	1.10	0.02
SC	1.02	0.26	1.36	0.05

6.6. Chapter summary

We find that MT provides consistent results for modeling homogenous induced stress in the pore space. As we also observed, it falls exactly between HS bounds. However, for modeling solid substitution MT might not be an ideal model unless induced stress in the pore space is homogeneous. That is almost never a case in real scenarios. Both SC and DEM perform better for modeling heterogeneous induced stress in the pore space. However, they do not cover the entire area of HS bounds, which might raise some issue with modeling certain pore geometries. Also, as we have seen in this study SC and DEM models do not model the way we assume. In the case where AR=1, SC and DEM ideally should have shown no heterogeneity in the pore inclusions, due to our assumption of isolated pores, however, what we find is not quite what we assume.

6.7. Acknowledgements

6.8.   References

Aksel, N., CE. Hubner, 1996, The influence of dewetting in filled elastomers on the changes of their mechanical properties: Archive of Applied Mechanics 66, 231-241, Springer-Verlag.

Berryman, J., 1980, Long-wavelength propagation in composite elastic media: Journal of Acoustic Society of America, 68, 1809-1831.

Berryman, J., 1992, Single-scattering approximations for coefficients in Biot's equations of poroelasticity: Journal of Acoustic Society of America, 91, 551-571.

Berryman, J., 1995, Mixtures theories for rock properties, in A Handbook of Physical Constants, T.J. Ahrens, ed. American Geophysical Union, Washington, D.C., 205-228.

Cleary, M. P, Chen, I.-W., & Lee, S.-M., 1980, Self-consistent techniques for heterogeneous media: ASCE Journal of Engineering Mechanics, 106, 861-887.

Comyn, J., 1997, Adhesion Science: Royal Society of Chemistry Paperbacks.

Connolly, P., 1999, Elastic impedance: The Leading Edge, 18(4), 438-452.

Dean, E., 1983, Elastic moduli of porous sintered materials as modeled by a variable-aspect ratio self-consistent oblate-spheroidal-inclusion theory: Journal of the American Ceramic Society, 66, 847-854.

Devaney, A., Levine, H., 1980, Effective Elastic Parameters of Random Composites: Applied Physics Letters, 37, 377.

Gaudig, W., R. Mellert, U. Weber, and S. Schmauder, 2003, Self-consistent one-particle 3D unit cell model for simulation of the effect of graphite aspect ratio on Young's modulus of cast-iron: Computational Materials Science, 28, 654–662.

Gosz, G., B. Moran, and J. Achenbach, J., 1991, Effect of a viscoelastic interface on the transverse behavior of fiber-reinforced composites: International Journal of Solids and Structures, 27, 1757-1765.

Hashin, Z., and Shtrikman, S., 1963, A variational approach to the elastic behavior of multiphase materials, Journal of the Mechanics and Physics of Solids, 11, 127-140.

Hashin, Z., 1991a, The spherical inclusion with imperfect interface: Journal of Applied Mechanics, 58, 444-449.

Hashin, Z., 1991b, Thermoelastic properties of particulate composite with imperfect interface: Journal of applied Mechanics and Physics of Solids, 39, 745-762.

Hashin, Z., 1992, Extremum principles for elastic heterogeneous media with imperfect interface and their application to bounding of effective moduli: Journal of applied Mechanics and Physics of Solids, 40, 767- 781.

Hashin, Z., 1983, Analysis of composite- a survey: Journal of Applied Mechanics, 50, 481-505.

Hill, R., 1952, The elastic behavior of crystalline aggregate: Proceedings of the Physical Society of London, A65, 349–354.

Kuster, G.T., and Toksoz, M.N., 1974. Velocity and attenuation of seismic waves in two-phase media. Geophysics, 39, 587-618.

Ledbetter, H. and M. Dunn, 1995, Microstructure and elastic-constant measurements of

two-phase materials: in Proceedings, IEEE Ultrasonic Symposium, 625-633.

Le Ravalec, M., and Y. Gueguen, 1996, High- and low-frequency elastic moduli for a saturated porous/cracked rock-differential self-consistent and poroelastic theories: Geophysics, 61, 1080-1094.

Lohe, D., O. Vohringer, E. Macherauch, 1983, Der Einfluß der graphitform auf den elastizitatsmodul von ferritischen Gusseisenwerkstoffen: Zeitschrift fur Metallkunde, 74, 265–273.

Mavko, G., Mukerji, T., and Dvorkin, J., 1998, The rock physics handbook, Cambridge University Press.

Norris, A., O., Sheng, and A. Callegari, 1985b, Effective-medium theories for two-phase dielectric media: Journal of Applied Physics, 57, 1990-1996.

Nur, A., G. Mavko, J. Dvorkin, and D. Galmudi, 1998, Critical porosity: a key to relating physical properties to porosity in rocks: The Leading Edge, 17, 357-362.

Saxena, N., and Mavko, G, 2014, Exact equations for fluid and solid substitution: Geophysics 79 (3), L21-L32.

Sheng, P., 1991, Consistent modeling of the electrical and elastic properties of sedimentary rocks: Geophysics, 8, 1236-1243.

Tong, J., Nan, C., 2001, Effect of inclusions shape on the effective elastic moduli for composites with imperfect interface: Acta Mechanica, 146, 127-134.

Torquato, S., 1991, Random heterogeneous media: microstructures and improved bounds on effective properties: Applied Mechanics Review, 44, 37-76.

Walsh, J.B., 1965, The effect of Cracks on compressibility of rock: Journal of Geophysics Research., 70, 381-389.

Wang, J., Karihaloo B., and Duan, H., 2009, Scaling laws for properties of materials with imperfect interfaces: in IUTAM Symposium on Scaling in Solid Mechanics, 10, 157-163.

Watt, P., 1988, Elastic properties of polycrystalline minerals: Comparison of theory and experiment: Physics and Chemistry of Minerals, 15, 579-587.

Wu, T.T., 1966. The effect of inclusion shape on the elastic moduli of a two-phase material. International Journal Solids Structures, 2, 1-8.

Zhang, M., Ebrom, D., McDonald, J., and Tatham, R., 1966, Comparison of experimental velocity measurements with theoretical results in a solid-solid composite material. Geophysics, 61, 1429–1435.